

Evaluation of the simulation of the 2006 California heat wave by WRF using satellite
and ground-based observations

By

AUDE VALADE

THESIS

Submitted in partial satisfaction of the requirements for the degree of

MASTER OF SCIENCE

in

Atmospheric Sciences

in the

OFFICE OF GRADUATE STUDIES

of the

UNIVERSITY OF CALIFORNIA

DAVIS

Approved:

Chair Richard Grotjahn

Susan L. Ustin

Shu-Hua Chen

Committee in Charge

2009

Table of contents

Abstract.....	1
Introduction.....	3
1. 2006 Heat wave over California	6
1.1. 500hPa Geopotential Height	6
1.2. Sea level pressure	10
1.3. 850hPa Air temperature.....	13
1.4. Soil variables and surface energy balance	16
2. Observational data	20
2.1. Surface station data	20
2.2. Satellite data	22
3. Description of the models.....	25
3.1. Weather Research and Forecasting Model.....	25
3.2. NOAA Land Surface Model.....	25
3.3. Land Information System	27
3.4. Experimental design	27
4. Results and discussion.....	30
4.1. Simulation of the diurnal cycle of air temperature by WRF	30
4.2. Spatial distribution of the temperature field: Simulation of Skin temperature	
46	
4.3. Relationship between Skin and Air temperature.....	63
5. Summary and Conclusions	77
6. References.....	80
6.1. Appendix1: Atmospheric humidity during the 2006 heat wave in California..	83

6.2. Appendix 2: Event identification.....	84
Long term daily means.....	84
Anomaly profiles.....	85
6.3. Appendix 3: CIMIS network of weather stations	88
6.4. Appendix 4: Offline spin-up simulation with the LIS.....	89

Abstract

Mesoscale modeling can be used in the forecasting of heat waves and in the understanding of their effects. The main goal of this study is to evaluate the ability of WRF-ARW to reproduce accurately an episode of extreme temperatures. The heat wave of July 2006 over California has been chosen as the period of study and two areas of different topography, land cover, and climate characteristics are focused on: the San Joaquin Valley and the Central Coast Valleys.

The simulated air temperature is compared with the CIMIS station data for evaluating the simulation of the diurnal cycle of air temperatures. The simulated skin temperature is compared with MODIS Land Surface Temperature retrievals to evaluate the spatial distribution of the error in the simulation of skin temperature. Wind field, land cover and soil moisture are used to help in the diagnosis of the simulation errors.

Two main questions are addressed:

How well can WRF reproduce the spatial and temporal characteristics of extreme heat events?

What is the relation between air and skin temperature?

The results show that the accuracy of the simulations varies with the time of the day, the day within the heat wave period, and the location of the station. The error in the simulation of air temperature is lower during the early hours of the daytime and increases during the afternoon as the sea breeze is overestimated by WRF. Within the areas covered by the observation stations, the bias is mainly positive, both during daytime and nighttime.

The spatial distribution of the error in the skin temperature field is consistent from day to day and depends on land cover type. Within the Central Valley, irrigated

agricultural areas show a warm bias both during daytime and nighttime while edge non-irrigated areas have a cold bias. The relationship between air and skin temperature depends on the response of both variables to wind field and radiation. In the San Joaquin Valley, their relationship varies between day and night whereas in the Central Coast Valleys it is similar.

Introduction

August 2003 in Europe and July 2006 in California are two record-breaking heat waves that contributed to raising the awareness on the risks of these extreme weather events. The intensity and duration of both of these events concurred to make them historical heat waves with many socio-economic consequences ranging from exceptionally high mortality rates and devastating forest fires to power outages and agricultural losses due to crop failures and livestock deaths (Fink et al., 2004; Kozlowski and Edwards, 2007).

The IPCC report of 2007 (IPCC, 2007) projects an increase in the frequency and intensity of extreme heat events over the century both in Europe and North America. Several studies have indeed showed that a warmer world would increase the risks of extreme heat events (Beniston, 2004; Gershunov and Cayan, 2008; Meehl and Tebaldi, 2004).

Two main factors are regarded as triggers to heat wave development: the synoptic upper-level state of the atmosphere and the soil moisture.

Heat waves are usually associated with upper-level high pressure patterns aloft (Grotjahn and Faure, 2008). The ongoing increase in greenhouse gases concentration in the atmosphere intensifies the current circulation patterns responsible for heat waves over Europe and North America (Meehl and Tebaldi, 2004). Recently, several studies have investigated the relation between negative soil moisture anomaly and heat wave development (Fischer et al., 2007b; Zampieri et al., 2009); and describe how soil moisture impacts the atmosphere through feedbacks involving cloudiness,

surface albedo, relative humidity and upper level atmospheric circulation, one of the key points being the role of soil moisture in partitioning latent and sensible heat fluxes.

The usual proxy for the study of heat waves in dry air regions such as California is surface air temperature. Surface air temperature (T_a) is related to the surface energy balance and the state of the atmosphere within the boundary layer. It is easily accessible and measured with high accuracy but the data are sparse and many areas are not covered.

Since the 1970s and the beginning of the satellite era, another thermal variable, the skin temperature, is available, with a worldwide coverage. The skin temperature (T_{skin} , also called Land Surface Temperature) is a radiative temperature derived from radiances measured by a radiometer remote from the surface. It is usually an average of various soil and canopy temperatures and depends on the surface properties more closely than T_a making it a key variable to the study of surface processes.

Mesoscale modeling can be used either as a forecasting tool or as an investigative one to understand better atmospheric processes. The Weather Research and Forecasting model (WRF) has proven able to predict weather patterns with good accuracy but the location of the study as well as the set of schemes and parameters chosen for the runs can greatly influence the distribution and magnitude of the errors (Case et al., 2008; Cheng and Steenburgh, 2005; Chiao, 2006; Fovell, 2008; Michelson and Bao, 2006; Sauter and Henmi, 2004). The simulation carried out in this study is challenging for the model because of the extreme temperatures in this unusual event (Fovell, 2008) and because of the complexity of the terrain in California (Sauter and Henmi, 2004).

The main goal of this study is to evaluate the ability of the WRF model to simulate accurately a heat wave event such as the 2006 heat wave over California both in terms of spatial distribution and daily temporal evolution. The use of station and satellite data gives a complementary set of observations with respectively high temporal and spatial resolutions. Also the study of the relation between the air temperature measured by station sensors and the radiative skin temperature retrieved from the satellites gives insights into the land-atmosphere interactions.

Section 2 briefly describes the 2006 heat wave over California and its causes. Section 3 and 4 present the models and observation datasets used for the experiments. The results are presented in section 5 with an emphasis on the diurnal cycle of temperatures, the spatial distribution of the skin temperature and the relation between skin and air temperature.

1. 2006 Heat wave over California

The first factor for the development of a heat wave is the synoptic situation. Extreme heat events are generally associated with upper level high pressure patterns aloft that generate large scale descending air and compressional heating.

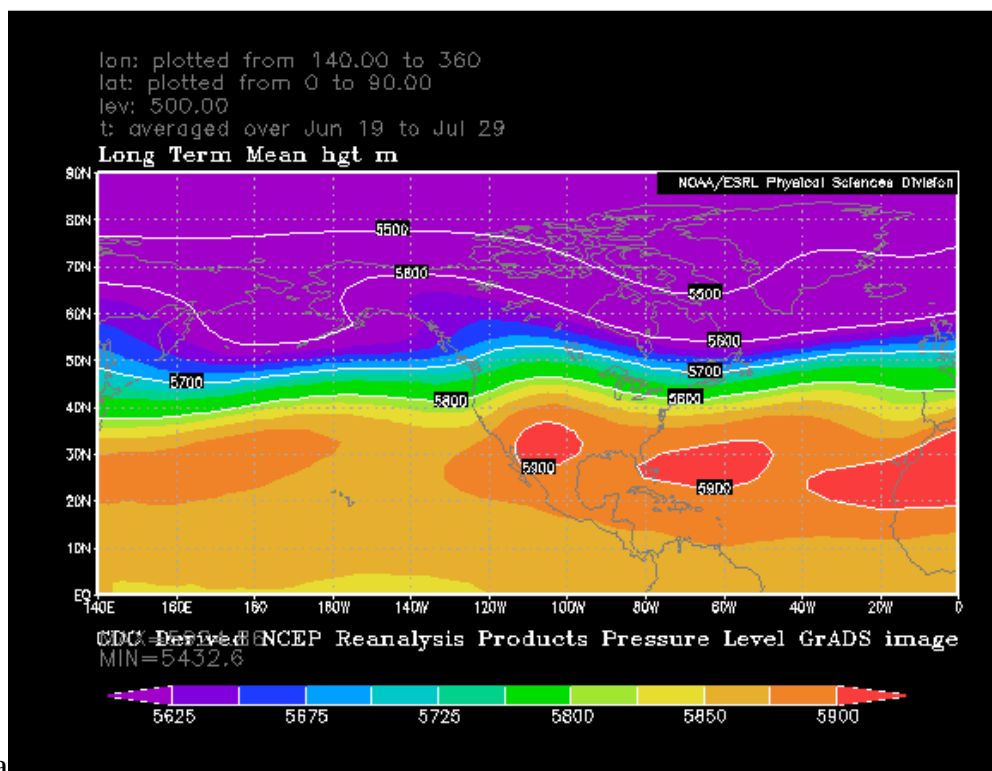
1.1. 500hPa Geopotential Height

Previous composite studies (Grotjahn and Faure, 2008) focusing on the prediction of the hottest heat waves, describe the upper level flow leading up to the onset of the event as the progressive development of a ridge-trough-ridge pattern located between the California coast and the mid-Pacific.

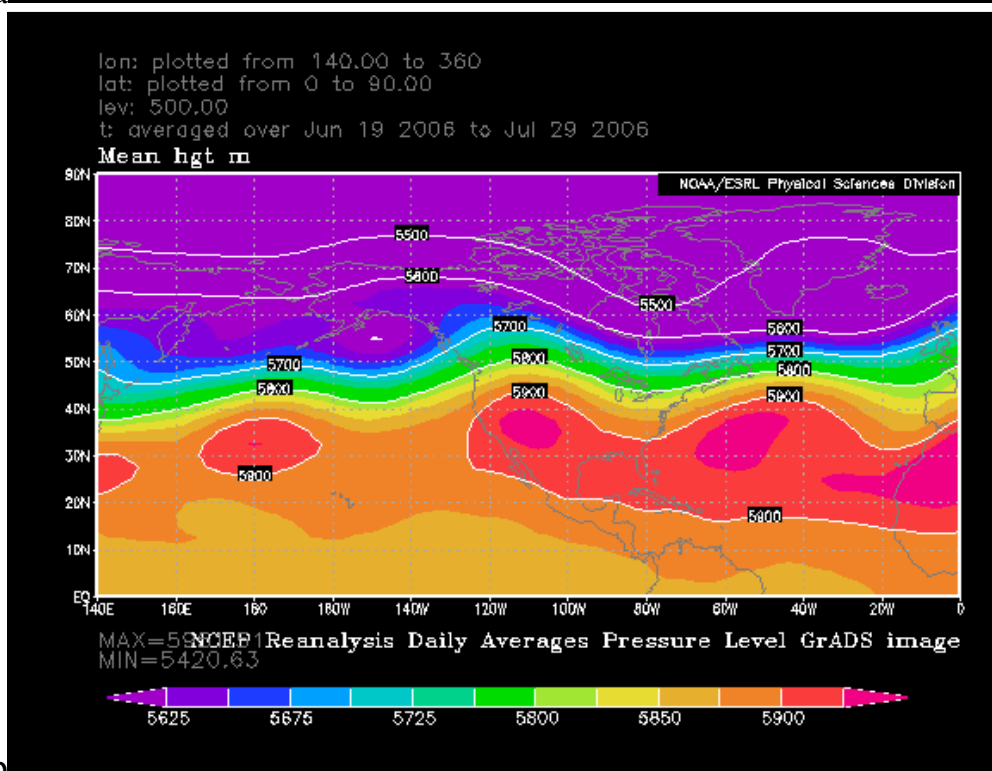
Figure 1(b) represents the synoptic situation averaged over the duration of the heat wave (from the 19th to the 29th of July 2006) for the 500hPa geopotential height compared with the climatology (Figure 1a)). Climatology of the 500hPa heights consists of a weak upper level high centered over New Mexico with westerly winds over California.

During the 2006 heat wave, the main upper level anomaly was the unusual strength and westward extension of this semi permanent summertime ridge (Figure 1a and b) associated with an upper level trough over the northeastern Pacific Ocean. This expansion of the upper level ridge above California resulted in the presence of a strong high pressure pattern aloft which increased the surface air temperature by enhancing sinking motion dynamically and by the topography that increased the compressional heating of the lower troposphere. The morning surface boundary layer inversion was amplified trapping more effectively the solar radiation thereby leading to the record high temperatures later in the day (Grotjahn, 2009). Another consequence was the reversal of the upper level flow over California from westerly to southerly

bringing the North American monsoonal moisture from Mexico and therefore raising the dew point temperatures and precipitable water values to unusual levels (Kozlowski and Edwards, 2007).



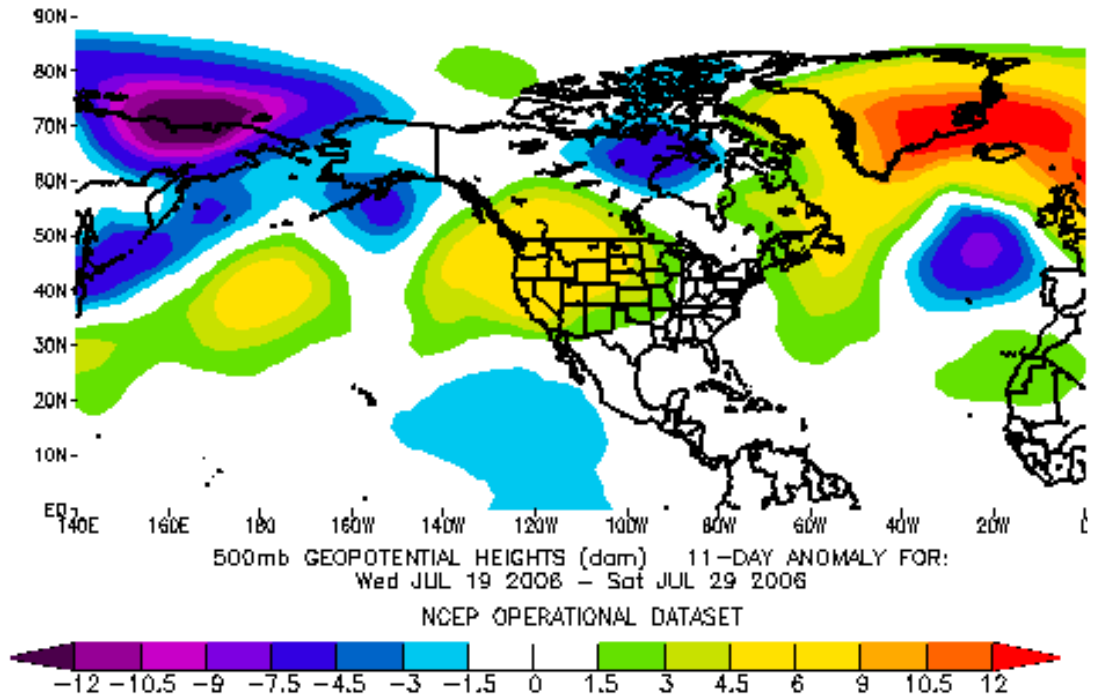
a



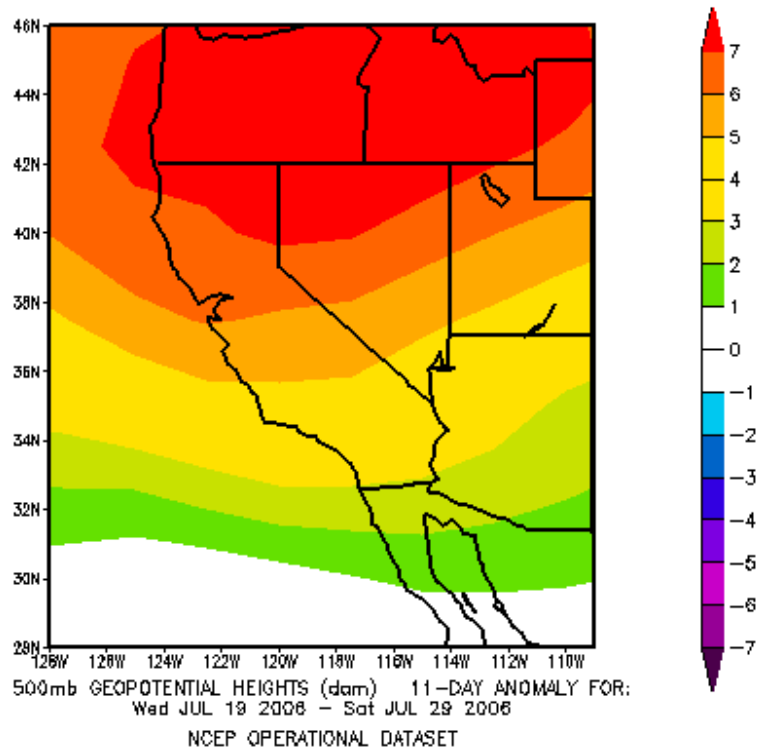
b

Figure 1: 500hPa Geopotential field.

a: climatology (daily long term mean) averaged from 19 July to 29 July, **b:** averaged over wave period, daily means averaged from 19 July to 29 July, figures from <http://www.esrl.noaa.gov/psd>.



a



b

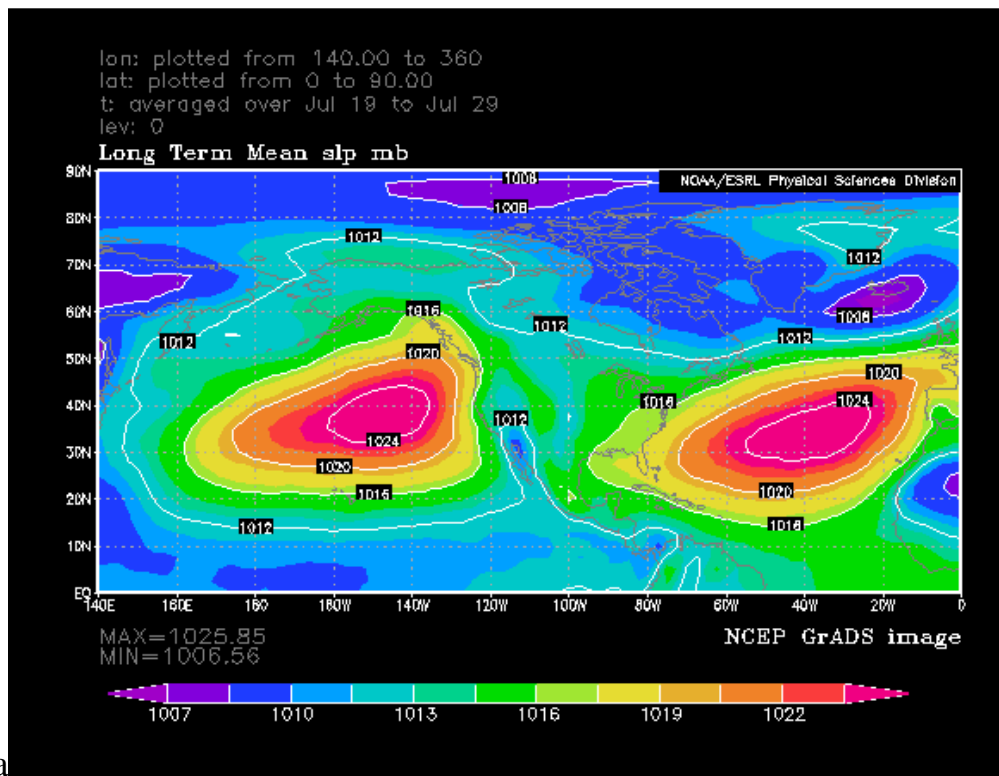
Figure 2: 500hPa Geopotential field anomalies averaged from 19 July to 29 July, figures from <http://www.esrl.noaa.gov/psd>

1.2. Sea level pressure

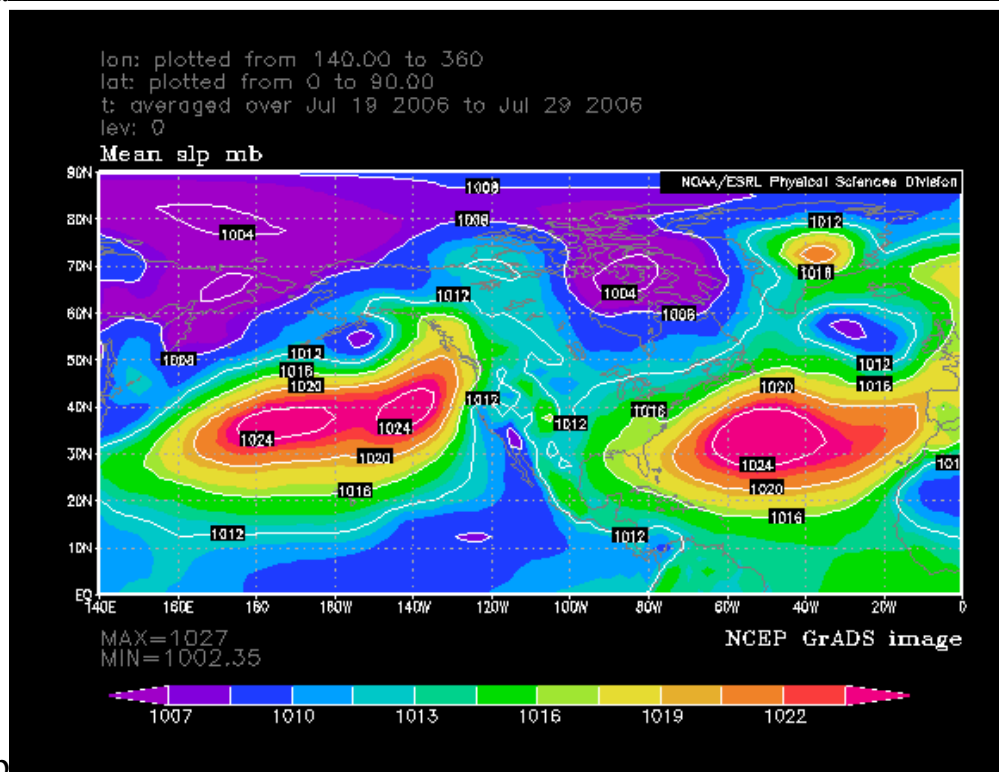
The climatology for the sea level pressure patterns, as illustrated in Figure 4(a), consists of a weak thermally-induced low along the Nevada and Utah border 500hPa Geopotential Height extending northward to the Great Basin and a high located in the northeastern Pacific Ocean bringing northwesterly winds to the West Coast of the United States.

Previous studies of composite anomaly maps found that heat waves over California are characterized by surface pressure patterns consisting of a surface high over the southern and central Great Plains, a surface low off the California coast, and a broad high west of the state of Washington's coast (Gershunov and Cayan, 2008). These features are similar in location to the climatological situation but are stronger, as seen for the 2006 event (Figure 4) with an especially deep thermal trough centered over southern California and Arizona.

This deep thermally induced low-pressure center along the Coast played a key role in the intensity of the heat wave. Indeed, the location of this trough generated a strong sea level pressure gradient (SLP) directed offshore and reversed the westerly flow to a weak easterly one. These two consequences combined to prevent the marine layer from penetrating inland at night, which is the typical response to the thermals generated inland during the day. Another factor is related to topography. As the easterlies flow down the Sierras, the air sinks, therefore warming up. This additional factor added to the absence of the typical sea breeze to advect the heat away yielded to an accumulation of the heat from day to day with less radiation needed to heat a layer already warm.

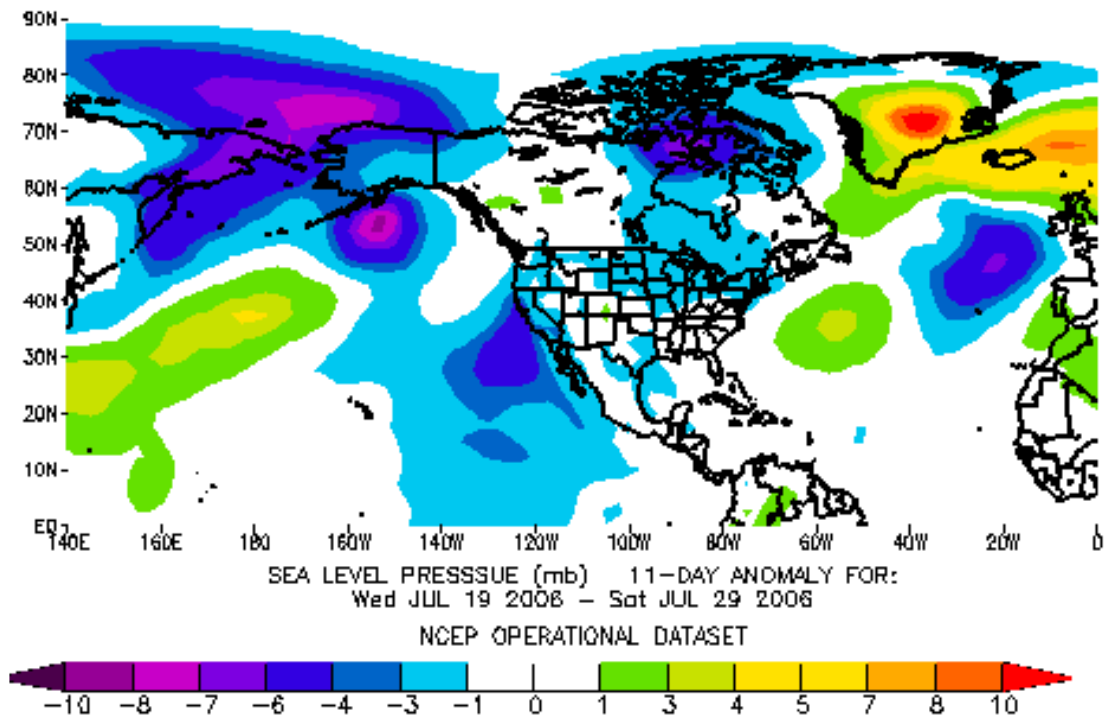


a

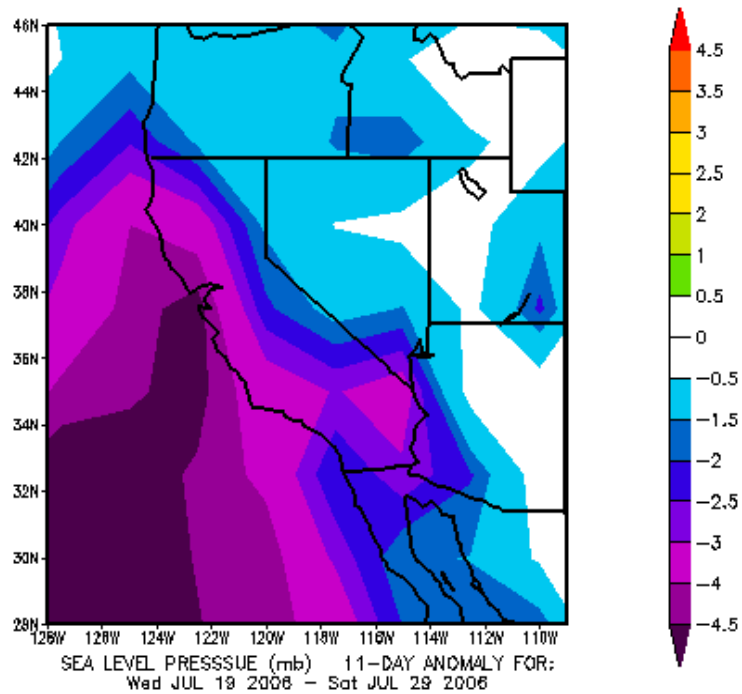


b

Figure 3: Same as Figure 1, for Sea level pressure



a



b

Figure 4: same as Figure 2 for sea level pressure

1.3. 850hPa Air temperature

Generally (i.e. climatology shown in Figure 6), the 850hPa temperature associated with the upper level geopotential height is higher over the southwestern US. during the heat wave of 2006, this high temperature area expanded to the west over California and strengthened. The highest anomaly is centered off the coast, a feature common to all of the hottest heat waves over the Central Valley (Grotjahn, 2009).

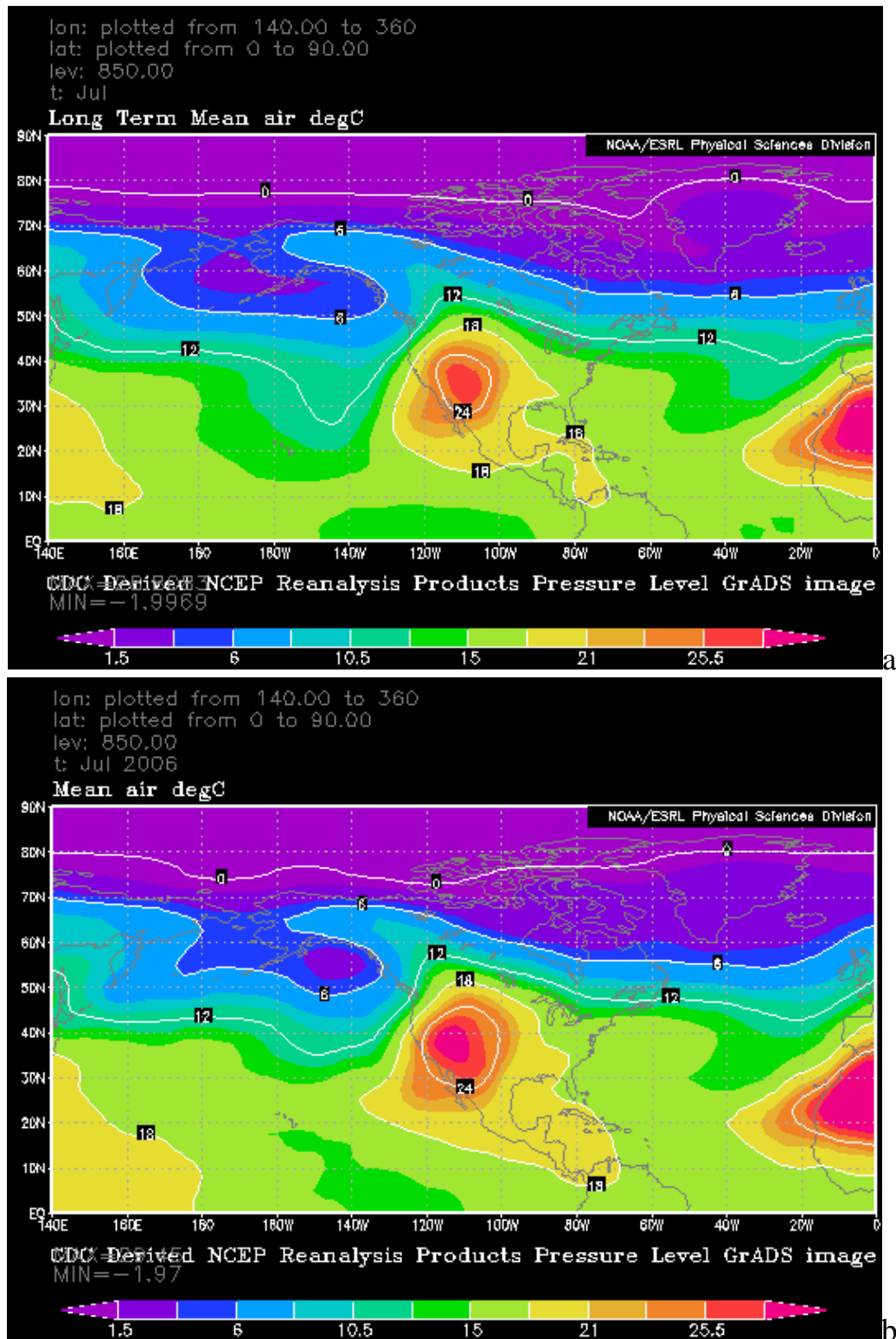
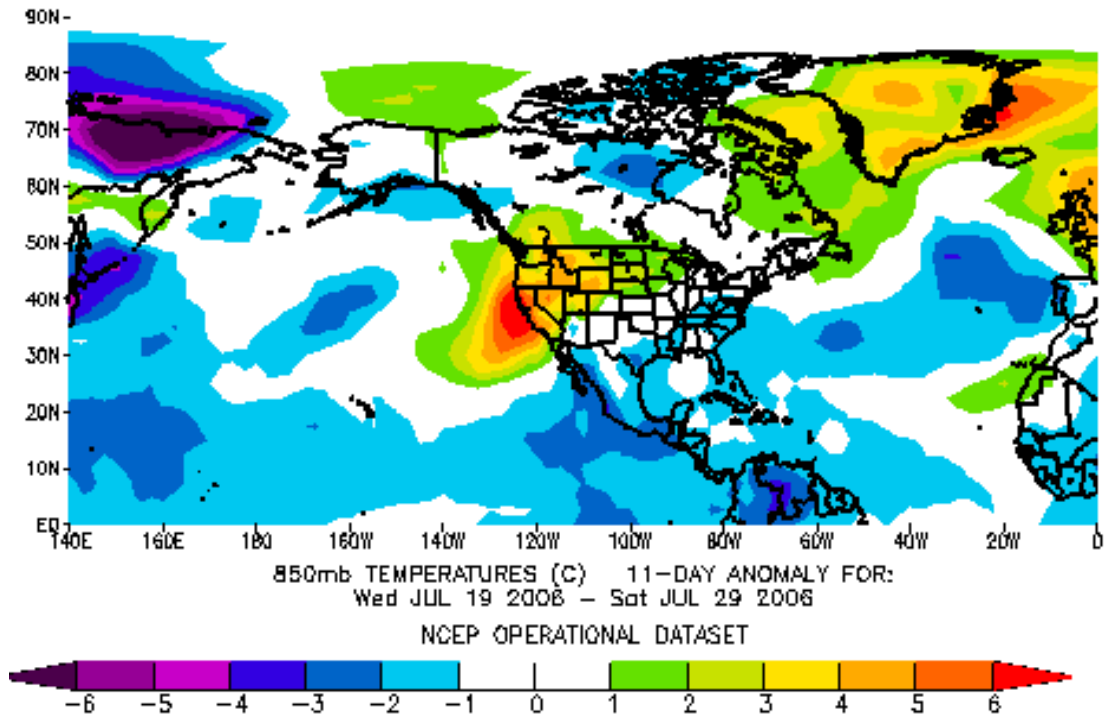
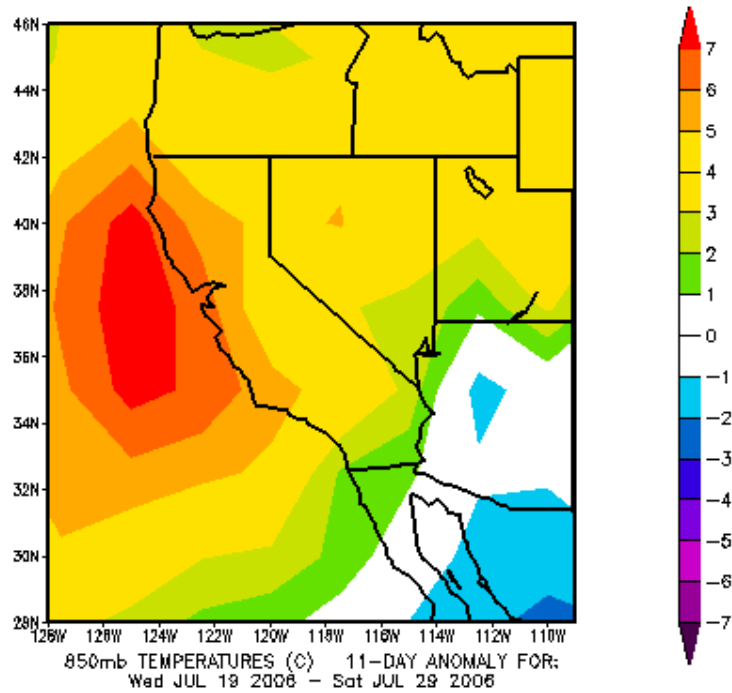


Figure 5: same as Figure 1 for 850 hPa air temperature



C



d

Figure 6: same as Figure 2 for 850 hPa air temperature

1.4. Soil variables and surface energy balance

If the synoptic patterns are presented as the triggers to the development of extreme heat events (Grotjahn and Faure, 2008), several recent studies have shown that land-atmosphere feedbacks contribute to the intensity and the persistence of the heat waves (D'Andrea, 2007; Fischer et al., 2007a; Fischer et al., 2007b; Zaitchik et al., 2006; Zampieri et al., 2009). Many hypotheses for these feedbacks are based upon a shift in the distribution of surface heat fluxes between latent and sensible parts (Fischer et al., 2007b; Zampieri et al., 2009) highlighting the role of the radiation budget at the surface. The net radiation available at the Earth's surface is the algebraic sum of the upward and downward shortwave and longwave radiations that reach the Earth's surface. A part of the Sun's (shortwave) radiation reaching the land is absorbed by the surface (downward, hence negative) (S_D), another part is reflected by the Earth's surface (upward, diffuse short wave radiation)(S_U). The Earth's atmosphere and surface emit longwave radiation, respectively downward (L_D) and upward (L_U).

The sum of all inputs and outputs radiation yields the net radiation flux at the surface:

$$(1) \quad R_{net} = S_D + S_U + L_D + L_U$$

The term L_U contains information about the skin temperature since, due to the very small heat capacity of the land, the variation in solar radiation along the day almost instantaneously results in a warming or cooling of the surface.

The term L_D (negative) is related to air temperature since it is the sum of all downward radiative emission by the atmosphere that reaches the surface.

R_{net} is almost constant and slightly negative during nighttime and positive with a peak near solar noon during daytime.

At the surface, this net radiative flux is partitioned between three heat fluxes:

E: latent heat flux (through evaporation). When evaporation is taking place, the surface loses energy to the air above (positive latent heat flux).

H: sensible heat flux (through warming of the atmospheric boundary layer). H is directly proportional to the difference between T_{skin} and T_{air} . When the surface is warmer than the air above, an exchange of heat takes place, through conduction firstly. Then the warmed air circulates upwards by convection.

G: conduction of heat into the ground

$$(2) \quad R_{\text{net}} = H + E + G$$

$R_{\text{net}} - G$ is the available energy at the surface, which is therefore partitioned into either sensible heat or evapotranspiration (Norman et al., 1995). If the soil is moist and/or covered with vegetation, much of the incoming energy goes into evaporating water (latent heat flux), leaving less to heat the air. If the soil is dry with no vegetation, the surface layer of the land loses more energy through sensible heat (assuming all radiative quantities being unchanged) and therefore increases the temperature of the air above. Thus, over a moist surface, the ratio is small, typically 0.1 over the sea, 0.2 over irrigated orchards or grass, and over dry areas it is larger, with typical values of 5 in semi-arid regions.

Several studies have recently tried to explain the mechanisms of heat waves development by investigating the surface energy budget. Using either satellite imagery based energy budgets (Zaitchik et al., 2006) or regional modeling (Fischer et al., 2007b; Zampieri et al., 2009), to investigate the processes and feedbacks involved during the 2003 heat wave in western Europe, they find that the hottest days in the heat wave do not have an unusual net radiation flux, but that drier soils caused by high temperatures and lack of precipitation result in an abnormal partitioning of

energy at the land surface with a shift towards sensible heat and away from latent fluxes therefore deepening the PBL height (and increasing the Bowen ratio). The decrease in latent heat flux and increase in sensible heat flux combine to heat the near-surface atmosphere and reduce the transfer of turbulent energy to the PBL. A dry soil warms quicker than a moist one, the longwave radiation from the ground towards the air is also increased, and therefore, assuming a surface energy balance, the available energy at the surface (R_{net-G}) is decreased along with the heat fluxes away from the surface ($H+E$). A deeper PBL height, associated with lower potential for convection (through a lower amount of Moist Static Energy per unit of PBL air (Hohenegger et al., 2009), adds up to the lower transfer of energy from the surface to the atmosphere to decrease the chance for convective precipitation. There is therefore a positive feedback with drier soils associated with lower precipitations.

Those studies focus on Western Europe and the mechanisms discussed before are deduced from observations and simulations specific to the European setting. The nature of land-atmosphere feedbacks described before depend greatly on the location and type of land cover (Adegoke et al., 2003) so that one has to be careful when considering these results for California. A soil moisture-temperature relationship exists in California too (Adegoke et al., 2003) but the precipitation and wind patterns are different. In Europe, average precipitation rates for the JJA period varies between 0 in Southern Spain to above 4mm/day over Switzerland, Austria and southern Germany, while California hardly receives any precipitation during the summer months allowing the soil in non-irrigated areas of the state to dry out. Therefore, the soil moisture is expected to be less of a factor for heat waves in California. The land-atmosphere feedbacks investigated over Europe however are relevant to the persistence and intensity of extreme heat events over California.

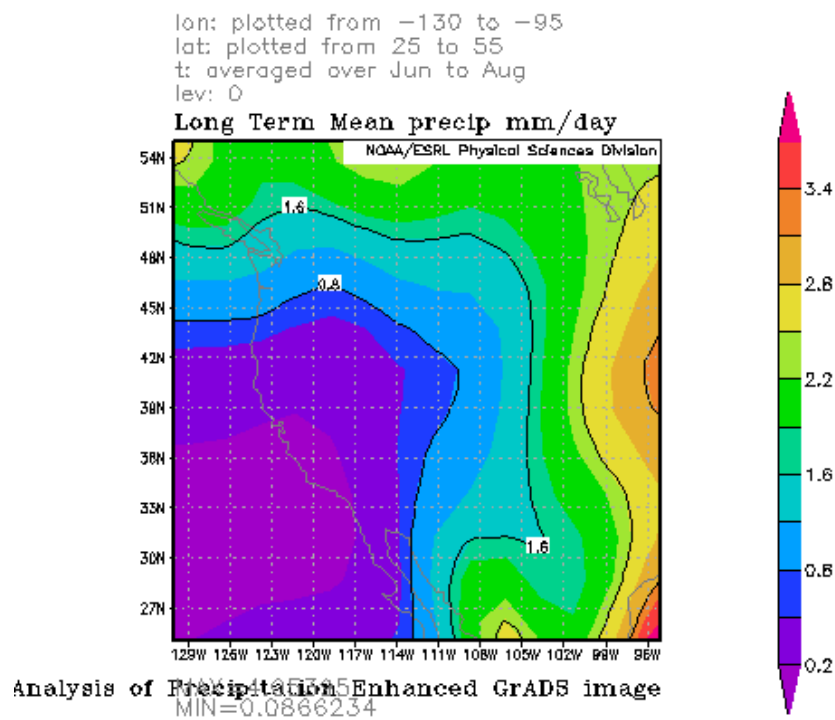
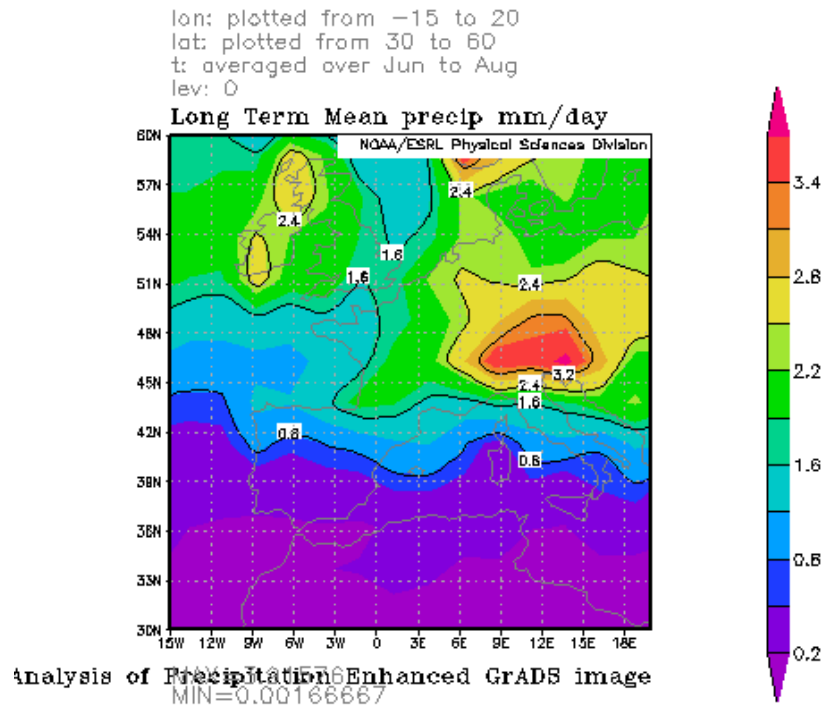


Figure 7: Climatological precipitation patterns for Europe (top) and California (bottom) averaged over the summer months (JJA). Note how California does not receive hardly any rain as opposed to Europe. Figures from <http://www.esrl.noaa.gov/psd>

2. Observational data

2.1. Surface station data

For this study, the temporal characteristics of the 2006 heat wave over California are identified based on the measurements from the CIMIS weather stations network (Hart et al., 2008).

The California Irrigation Management Information System (CIMIS) program was introduced by the California Department of Water Resources and the University of California, Davis in 1982. The original goal of the CIMIS network was to provide evapotranspiration data to California's growers to improve water use by helping irrigation scheduling. There are over 130 computerized weather stations located at key agricultural and municipal sites throughout California providing comprehensive and timely weather data to a large users group including farmers, firefighters, engineers, researchers, meteorologists.

The hourly data that are used for this study are hourly averages of 60 consecutive sensor readings.

The stations are grouped into Evapotranspiration regions with homogeneous characteristics. These regions are described in Figure 8. The following study focuses on two of these regions: the San Joaquin Valley (SJV) and the Central Coast Valleys (CCV). The Central Valley is surrounded by mountains (Tehachapi Mountains along the south edge, coastal ranges along the west side, the Sierra Nevada Mountains on the east side, and the Cascades on the north end) and therefore, with a few exceptions is largely protected from the penetration of the sea breeze. On the contrary, the Central Coast region is directly exposed to the maritime airflow



Figure 8: CIMIS Evapotranspiration regions. Each number represents the identifying number for a station. Stations located within a same Evapotranspiration region have the same color.

2.2. Satellite data

The spatial analysis of the heat wave will be performed with the help of the MODIS Level 2 Land Surface Temperature product.

Two Moderate-Resolution Imaging Spectroradiometer (MODIS) sensors are currently operating onboard the polar orbiting satellites Aqua and Terra. Each of these satellites has two overpasses every day (one ascending and one descending) leading to a MODIS temporal resolution of 4 overpasses a day. For California, the times of the overpasses are around 600UTC (2300Local Time) and 1800UTC (1100LT) for Terra and around 1000UTC (300LT) and 2200UTC (1500LT) for Aqua. It is noteworthy that these times, especially the Aqua ones are close to the times of maximum and minimum temperatures and are therefore very relevant to the study of heat waves.

MODIS is a 36-band spectroradiometer measuring visible and infrared radiation, at different resolutions. The first two bands cover the visible red and near infrared and have a 250m pixel size. The next five have 500m spatial resolutions and cover several bands in the visible, near infrared and Shortwave Infrared spectral bands. The other spectral channels have a 1 km resolution and include several bands in the visible, near-infrared, middle infrared and thermal infrared for ocean and atmosphere studies and land thermal monitoring. The swath width covers 2300km and provides daily world-wide observations (Chuvienco and Justice, 2008).

The MODIS Land Surface Temperature (LST) is retrieved from Thermal Infra-Red (TIR) data. It is defined as the radiation emitted by the land surface observed by MODIS at the instantaneous viewing angle. Its retrieval is based upon a split-window technique first developed to retrieve sea surface temperatures from satellite data

making use of the differential absorption in two adjacent infrared channels. One of the major limitations to thermal infrared imagery is cloud contamination since the thermal Infrared signal cannot penetrate clouds to reach the satellite. In order for the LST not to be mixed with cloud-top temperature, MODIS LST is only retrieved in clear-sky conditions. The detection and elimination of partly or totally cloudy pixels is performed through the use of cloud detection algorithms, which usually perform tests on several visible and IR channels.

Satellite-retrieved land temperature has multiple uses. First of all, it can be used to determine the spatial variations and boundaries of near surface temperature fields. Color enhancements provide a quick and easy way of tracking changes in the temperature field over time. Also, because this temperature corresponds exactly to the temperature of the interface between land and atmosphere, it is related with, and contains a lot of information about the processes of exchange of energy, and water between land and air.

For this study we use the level 2 MYD11_L2/MOD11_L2 Aqua/Terra products generated from the MODIS sensor radiance data product (MOD021KM), the geolocation product (MOD03), the cloud mask product (MOD35_L2), the quarterly landcover (MOD12Q1), and the snow product (MOD10_L2). The output file contains Scientific Datasets (SDS) of LST, quality assurance (QA), error in LST, emissivities in bands 31 and 32, viewing zenith angle and time, latitude and longitude (each set of latitude and longitude for every 5 scan lines and 5 pixels), local attributes, and global attributes. This LST product is generated by the generalized split-window LST algorithm (Wan and Dozier, 1996).

This algorithm utilizes the longwave window channels 31 and 32 and coefficients varying with the viewing angle. The split-window algorithm equation is:

$$T = C + \left(A_1 + A_2 \frac{1 - \varepsilon}{\varepsilon} + A_3 \frac{\Delta \varepsilon}{\varepsilon^2} \right) \frac{T_{31} + T_{32}}{2} + \left(B_1 + B_2 \frac{1 - \varepsilon}{\varepsilon} + B_3 \frac{\Delta \varepsilon}{\varepsilon^2} \right) \frac{T_{31} - T_{32}}{2}$$

$$\varepsilon = 0.5(\varepsilon_{31} + \varepsilon_{32})$$

$$\Delta \varepsilon = \varepsilon_{31} - \varepsilon_{32}$$

T refers to the skin temperature. The subscript 31 and 32 refer to the channels used for the measurement, so here T_{31} and T_{32} are the brightness temperatures measured by the channels 31 and 32.

The emissivities ε are estimated from land cover types and may vary even within a land cover type, for example because of different soil moisture contents. A_i , B_i , and C are coefficients computed from the transmittance and emissivity of the land surface and depend on viewing zenith angle (in range of 0-65degrees) and on ranges of the air surface temperature and column water vapor. Only pixels identified as clear-sky are processed.

The spatial resolution of the products retrieved with this method is 1km.

3. Description of the models

3.1. Weather Research and Forecasting Model

Temporal and spatial resolution along with forecasting possibilities make models essential to the understanding and capture of weather events such as heat waves.

The Weather Research and Forecasting Model (WRF) is a state of the art mesoscale atmospheric simulation model designed for use both for research and operational purposes. It solves the compressible non-hydrostatic Euler equations in flux form with mass-based terrain-following vertical coordinates (Skamarock et al., 2005).

Previous studies have shown that WRF's output temperature fields are less accurate for summertime high temperature situations (Caldwell et al., 2009; Fovell, 2008). Cheng and Steenburgh (2005) suggest that an improvement in the soil initialization of the LSM would lead to more accurate weather forecasts.

This study aims at evaluating the performance of WRF at reproducing the 2006 California heat wave. The WRF model output variables 'Temperature at 2m' and 'Skin Temperature' are especially relevant and will be compared with observations to assess the accuracy of WRF predictions.

3.2. NOAH Land Surface Model

As described in Section 2 the processes involved in the development of heat waves are the result of a complex contribution of soil states and atmospheric dynamics

through water and energy fluxes at the surface. Therefore, the way the land surface and subsurface is modeled is crucial for the simulation of a heat wave.

Atmospheric models such as WRF are coupled with Land Surface models (LSM) such as the community NOAH Land Surface Model to predict surface fluxes used in the simulation of atmospheric variables.

A LSM requires 3 types of input: Initial conditions (initial state of the land), boundary conditions (upper and lower fluxes and states also called atmospheric and soil forcings) and parameters (functions of soil type, vegetation and topography).

From these inputs, LSMs solve the governing equations of the soil-vegetation-snowpack medium and predict the fluxes and soil states.

NOAH calculates all the soil variables such as soil temperature and moisture but also the interface quantities like sensible and latent heat fluxes, evapotranspiration flux from the vegetation, and fluxes at the canopy level.

Skin temperature is calculated following (Mahrt and Ek, 1984) by applying a single linearized surface energy balance equation, given by:

$$T_{\text{skin}} = \frac{R_n - \lambda E - G}{\rho C_p C_h |U_a|} + T_a$$

(Where T_{skin} is the skin temperature, R_n is the net radiation (W.m^{-2}), λE is the latent heat flux (W.m^{-2}), G is the ground heat flux (W.m^{-2}), ρ is the air density (kg.m^{-3}), C_p is the air heat capacity ($\text{J.m}^{-3}.\text{K}^{-1}$), C_h is the surface exchange coefficient for heat and moisture (dimensionless), $|U_a|$ is the surface layer wind speed (m.s^{-1}), T_a the air temperature.)

This equation is an expression of the surface energy balance expanded such that the skin temperature term appears.

3.3. Land Information System

The Land Information System (LIS) is software developed by the Hydrologic Sciences branch at NASA's Goddard Space Flight Center designed for high performance land modeling and data assimilation (Kumar et al., 2006). The goal is to integrate satellite data, ground observations data and modeling reanalyses data into land surface models to produce land surface variables such as soil moisture, evaporation or heat fluxes. Its high flexibility allows the choice of several LSMs. We use the community NOAH Land Surface Model coupled with WRF in our experiments.

LIS can be run offline using atmospheric forcings (e.g. North American Land Data Assimilation System (Case et al., 2008; Mitchell et al., 2004) to drive one of the available community models (e.g. NOAH).

LIS can also be run coupled with WRF to integrate the soil quantities into the atmospheric modeling then used as the forcing to the LSM.

LIS has been tested for its abilities to reproduce soil moisture at regional scale and the results show that small differences in soil moisture can lead to several degrees of difference in the simulated 2m-temperature field (Mostovoy and Anantharaj, 2007).

3.4. Experimental design

The simulations in this study are carried out using the ARW (Advanced Research WRF) dynamical core of the version 2.2 of the Weather Research and Forecasting Model developed at the National Center for Atmospheric Research (Skamarock et al., 2005).

Four soil layers and twenty-seven levels are considered on the vertical. The parameterization is chosen following Case et al. (2008).

The WSM 6-class scheme is chosen for microphysics (Hong and Lim, 2006), MYJ PBL(Janjic, 2002) and NOAH LSM surface schemes (Ek et al., 2003; Gershunov et al., 2006) are respectively used for planetary boundary layer and surface physics. No cumulus parameterization is used, all the convective processes are explicitly solved by the WSM6 microphysics scheme and model dynamics. Rapid Radiative Transfer Model (RRTM) longwave (Mlawer et al., 1997) and Dudhia (1989) shortwave radiation schemes are chosen.

The domain of the run has been chosen to encompass nearly all of California at a resolution of 4km (Figure 9). A 10-day simulation was run starting the 19th of July 2006 at 00UTC.



Figure 9: WRF domain, resolution of 4 km

The initial and boundary conditions are given by the 1.0x1.0 degree 6-hourly NCEP Global Forecast System Final Analysis data (GFS-FNL available at <http://dss.ucar.edu/datasets/ds083.2/data/>) and interpolated to the domain grid using the WRF typical initialization utilities within the WRF Pre-processing system (WPS). The static fields and grid parameters are first defined. Then, the boundary and initial

meteorological fields are decoded from the grib format. The outputs of both of these steps are used to interpolate the data onto the domain grid, horizontally and then vertically.

In order to evaluate the soil moisture field used by WRF for its simulation, the LIS framework is used to run the Noah LSM offline and generate high-resolution land surface fields for comparison. A preliminary analysis consists in the determination of the necessary length of the offline run for the simulated soil to reach equilibrium. Spin ups of different time lengths are run and the differences between the outputs are calculated (method and results in Appendix4.). It is found that an offline run of 24 months is sufficient for the soil to reach equilibrium and is therefore used to generate the control soil moisture fields.

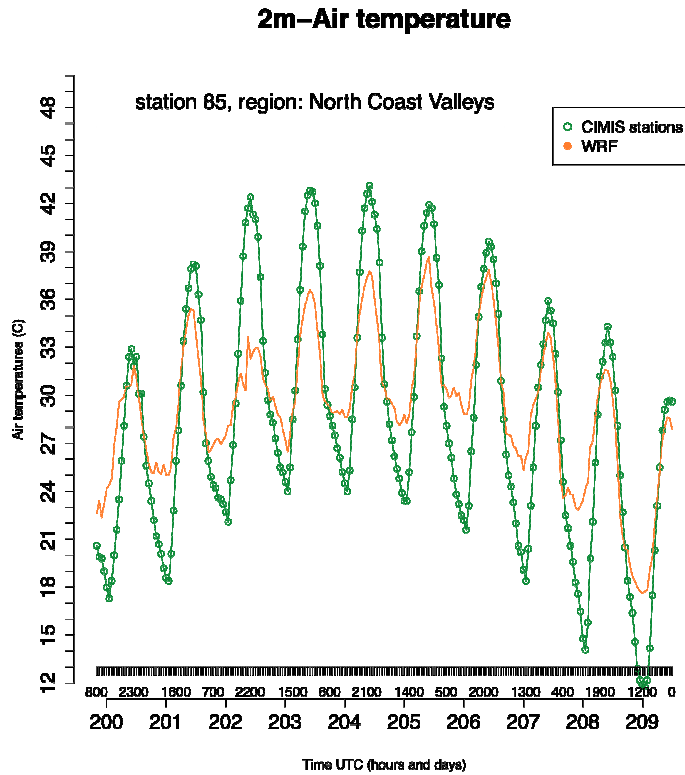
4. Results and discussion

4.1. Simulation of the diurnal cycle of air temperature by WRF

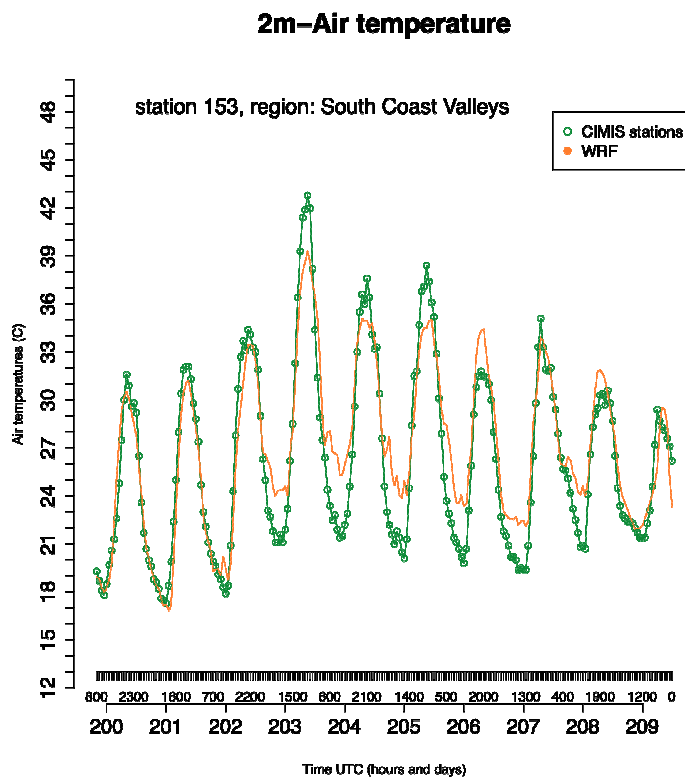
The diurnal cycle of air temperatures at 2m above the surface (T_a) results from a complex combination of processes involving the incoming solar radiation, the atmospheric boundary layer and the land surface. Its simplest conception is as a balance between incoming solar radiation, surface heat fluxes and outgoing longwave radiation. When the sun rises, the downward radiation exceeds the upward fluxes and the land stores energy, therefore increasing its temperature. In the afternoon, the downward solar radiation decreases and is exceeded by the upward heat fluxes. The land releases energy and cools down as well as the air above. The characteristics of this cycle vary spatially for several reasons. Soil moisture can be one. Arid areas have small latent heat fluxes causing a larger part of the energy received at the surface to be released as sensible heat fluxes and therefore making surface temperature more sensitive to solar forcing. Other reasons include differences in plant density, health of the vegetation, and differences in emissivity from soil surfaces of different chemical composition. Spatial variability of the diurnal cycle of temperatures is also due to differences in emissivity/absorptivity and heat capacity at the surface. Water bodies for example have a large heat capacity resulting in a small amplitude diurnal cycle of temperatures in the coastal areas. The high temporal resolution of the stations measurements allows evaluation of the full diurnal cycle simulated by WRF. As described in section 3.4, WRF has been run for a 10-days period centered on the peak of the heat wave, between the 19th and the 29th of July 2006.

First, the spatial variability of the diurnal cycles and the accuracy of the simulations are analyzed station by station. Then the regional behavior of the diurnal cycles is studied by averaging them over two of the Reference evapotranspiration regions defined by the CIMIS network: the San Joaquin Valley and the Central Coast Valleys (Figure 8 for the stations included in each region). The WRF runs described in this section are the output of a single integration of WRF of 10 days starting on the 19th of July 2006, 0GMT and ending on the 29th of July 2006, 0GMT.

Individual stations can have very different diurnal cycles but the way WRF captures the hourly temperature evolution has common features between stations. When considering all of the regions of the CIMIS network (116 stations), the daily minimum temperature is overestimated by WRF for all of the stations, and the daily maximum temperature is overestimated for 91 stations out of 116. The stations where WRF simulates a colder daily maximum temperature than observed at the stations are generally located in the coastal areas. Figure 10 shows two examples of such stations. It is noteworthy that some stations have a wide range of DTR that WRF has difficulties capturing as illustrated in Figure 10(b) with an example of station located in the South Coast Valleys region (station number 153). At this station, the DTR ranges between 10C on the 27th of July (Julian day 208) and 21C on the 22nd of July (Julian day 203) whereas WRF simulates a DTR ranging between 10C and 15C). Other examples of stations where WRF has difficulties capturing highly variable diurnal cycles of temperatures are illustrated with Figure 12, for two more coastal stations: station number 184 located in the South Coast Valleys region and station number 19 located in the Monterey region. Indeed, for stations directly exposed to the marine influence (coastal areas), the time series of air temperature are more erratic and WRF has problems capturing the high frequency temperature variations.



a

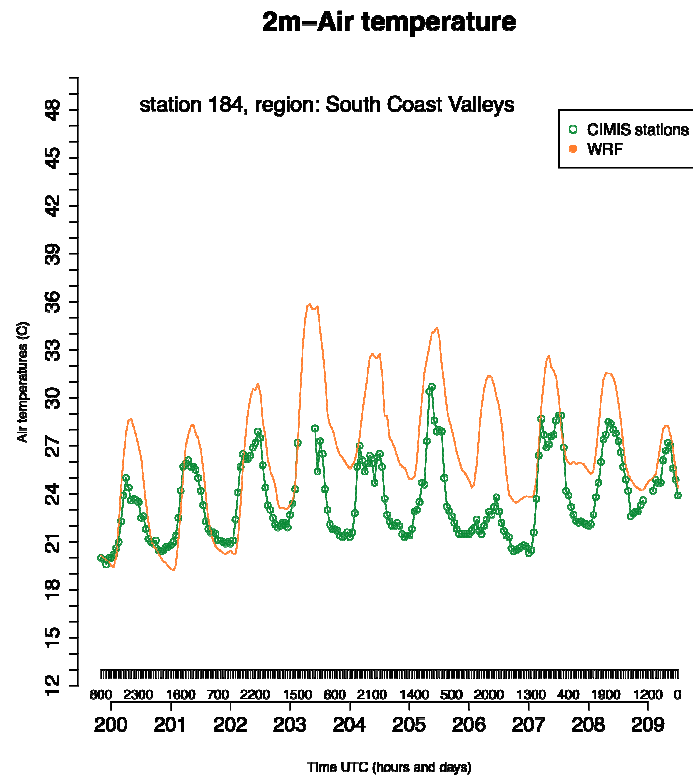


b

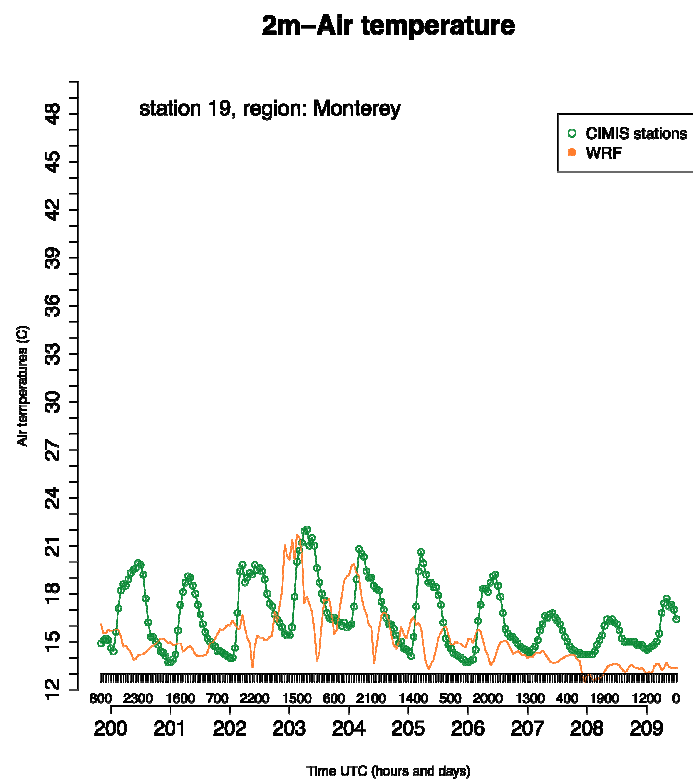
Figure 10: Comparison of station and modeled 2m-air temperature for two examples of underestimation of daily maximum of 2m-air temperature by WRF: (a) station number 85 in the North Coast Valleys region and (b) station number 153 in the South Coast Valley regions. (c) Locations of the stations. Daily minimum are always overestimated.



Figure 11: Locations of CIMIS stations 85 and 153



a



b

Figure 12: Comparison of the observed and simulated air temperatures for coastal stations (a: station number 184, South Coast Valleys, b: station 19, Monterey). The observed temperature field (green line with circles) shows high frequency variability that is not captured by WRF.



Figure 13: Locations of CIMIS stations 19 and 184

The accuracy of the WRF simulations varies from one station to the other. However, within a region, the errors have some common features. These features are studied more in details for two regions: the San Joaquin Valley and the Central Coast Valleys.

The San Joaquin Valley and the Central Coast Valleys regions differ by their topographical and meteorological characteristics: the Central Coast Valleys are highly influenced by the marine air and the air channeling whereas the San Joaquin Valley is flat and protected from the ocean influence by several mountain ranges and therefore is most of the time protected from it. Figure 14 and Figure 15 show, for the San Joaquin Valley and the Central Coast Valleys respectively, the region-averaged hourly temperatures measured at the CIMIS stations and simulated by WRF, as well as the time series of the root mean square errors for the stations of the region (RMSE).

The RMSE is calculated as follows:

$$(4) \quad RMSE = \sqrt{\frac{1}{N} \sum_N (T_i - \hat{T}_i)^2}$$

with T_i the observed temperatures and \hat{T}_i the modeled temperatures, N the number of observations used for the calculation of the RMSE.

For both regions illustrated in Figure 14 and Figure 15, (San Joaquin Valley and Central Coast Valleys), on average, WRF captures most general properties, such as the increasing (followed by decreasing) temperatures, the times of minimum and maximum temperatures, the amplitude of the diurnal temperature range (DTR) and the overall shape of the evolution of the temperatures. However, in both of these regions the decrease in temperature between the late afternoon and the time of minimum temperature happens later in the WRF simulations compared to the observations.

The 2m-air temperatures (T_a) in the San Joaquin Valley and the Central Coast Valleys regions are both consistently overestimated by WRF. In the San Joaquin Valley, the overestimation of the minimum temperature ranges between 1 and 3C, and the overestimation of the maxima between 2 and 4C. In the Central Coast Valleys, the overestimation of the temperatures by WRF is more important and has a larger variability between days since it ranges between 2 and 9C for the minima and between 0 and 6C for the maxima. The analysis of the RMSE for the two regions of focus (San Joaquin Valley, Figure 14, and Central Coast Valleys, Figure 15) reveals that the error in the WRF simulation compared to the station-based observations depend both on the time of the day and on the day itself within the heat wave period. Over much of the simulation in the San Joaquin Valley, Figure 14 shows a consistent diurnal pattern of the error during the day. The temperatures are close to the observations during the period of increasing temperature in the morning. The decrease in temperature is triggered earlier in the observational data than in the modeled ones and therefore the RMSE increases after the maximum is reached in each cycle during which it remains stable. This diurnal pattern is not as clear for the Central Coast Valleys region. Local peaks in the RMSE are in phase with times of minimum temperatures but the error seems more influenced by the development of the heat wave than by these diurnal variations. Along the heat wave, the error increases from a local minimum of 1C on the 19th of July (Julian day 200) and a local maximum of 12C on the 23rd of July (Julian day 205) and then decreases to 2C on the 28th of July (Julian day 209). The maximum RMSE reached in the San Joaquin Valley is also 12C on the 23rd.

Some of these error patterns can be related with the results of the wind simulation. Figure 18 and Figure 19 show the time series of the wind components averaged by

region. Because we are interested in the wind resulting from the sea/land breeze, we are looking at the West-East component of wind in the Central Coast Valleys (wind orientated along the pressure gradient resulting from the differential land/sea heating) and North-South component of wind in the San Joaquin Valley (channeled from the Delta Bay down the San Joaquin Valley). Figure 16 and Figure 17 represent respectively the observed and simulated wind fields. In both regions, the daily wind pattern is very clear. In the morning around 1300GMT (6am LT), the land/sea differential heating results in a pressure gradient with lower pressure inland and higher pressure offshore. This gradient generates the sea breeze seen in Figure 18 as the northerly wind channeled into the San Joaquin Valley, and in Figure 19 as the westerly wind coming more directly from the Pacific. The maximum wind speed is reached around the time of maximum temperature, 2200GMT (3pm LT) and then decreases and eventually reverses if the pressure gradient reverses its direction such as to generate a land breeze at night between around 600GMT (11pm LT) and 1300GMT (6am LT). In the San Joaquin Valley, WRF tends to overestimate the sea breeze phenomenon, both in amplitude and duration. The triggering of the sea breeze in the morning simulated by WRF is close to the observed values. However, the diminution of the southward wind in the evening starts later than in the observations and does not reach a minimum until the sea breeze starts again on the next day, as opposed to the observed wind field where the wind speed remains minimum all night long. This lag between the simulated and observed decay of the breeze corresponds to the lag between the simulated and observed decrease in temperature during the evening as seen in Figure 14. The minimum and maximum wind speeds are both overestimated and the maximum RMSE is found during the time of decreasing wind speed.

RMSE hourly averaged over the stations of San Joaquin Valley

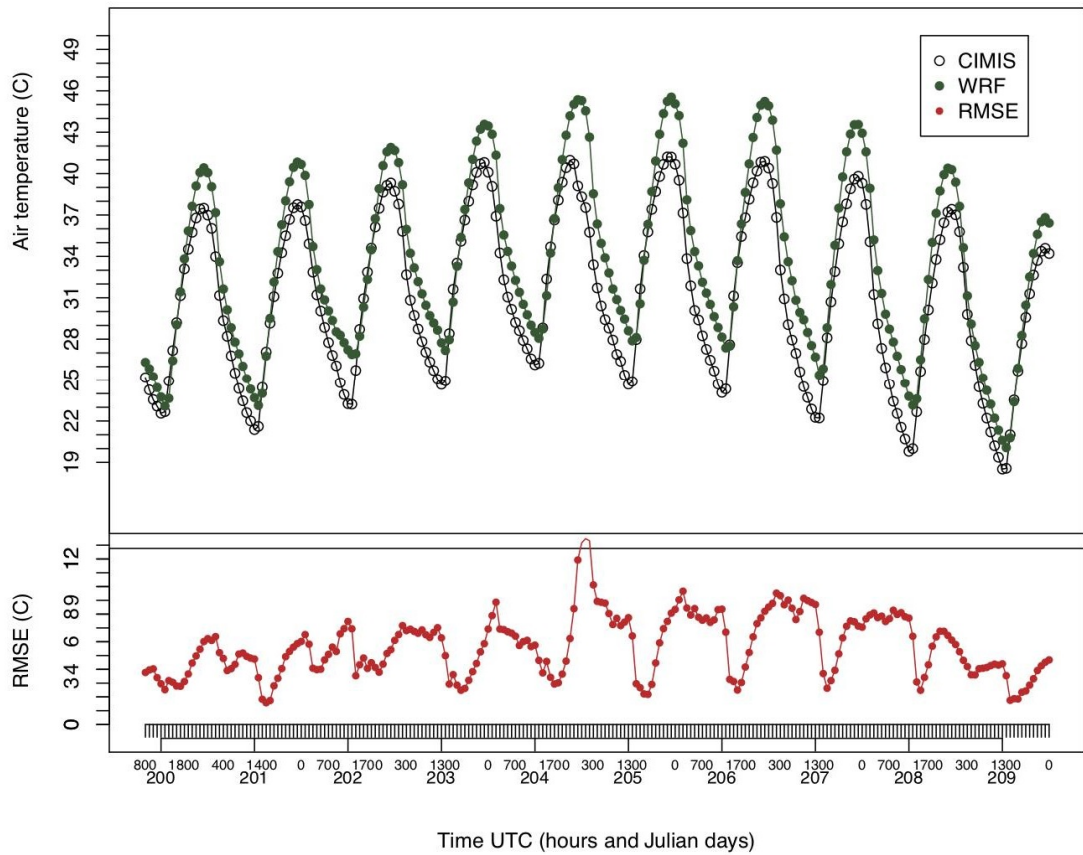


Figure 14: Comparison of WRF and CIMIS temperature cycles during the heat wave. In black, hourly CIMIS observations; in green: WRF simulations of the 2m-Air temperature; in red, RMSE. The hourly temperatures are averaged for 26 stations within the San Joaquin Valley region. The WRF values at the locations of the stations are retrieved using a nearest-neighbor method.

RMSE hourly averaged over the stations of Central Coast Valleys

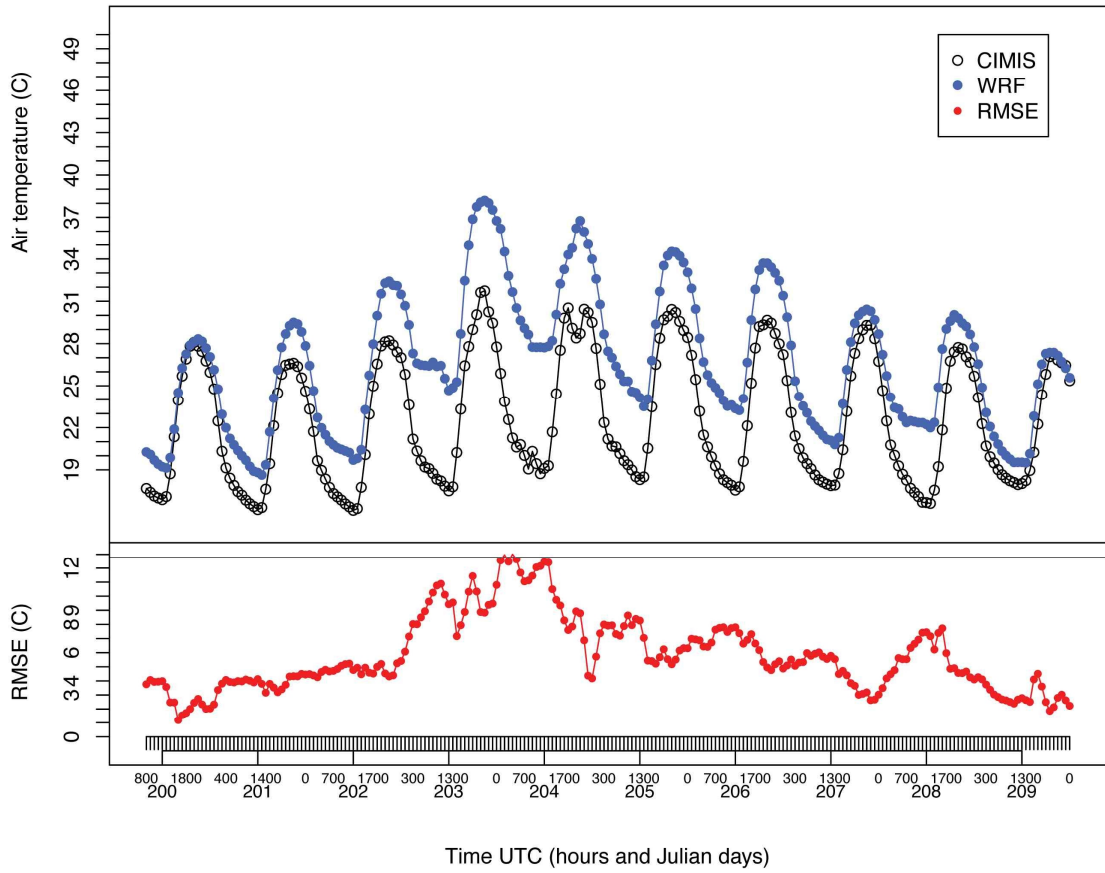


Figure 15: Comparison of WRF and CIMIS temperature cycles during the heat wave. In black, hourly CIMIS observations; in blue: WRF simulations of the 2m-Air temperature; in red, RMSE. The hourly temperatures are averaged for 10 stations within the Central Coast Valleys region. The WRF values at the locations of the stations are retrieved using a nearest-neighbor method.

Also, in the San Joaquin Valley, the land breeze is generally weak or non-existent except on the two nights (203 and 204) before the hottest day (204) when we can see a weak southerly flow at night. On these same days, the observations show the weakness of the sea breeze (Julian day 204, maximum southerly wind speed: 0.5m/s) whereas WRF simulates a wind pattern similar to the other days (3.5m/s).

In the Central Coast Valleys, the sea breeze occurrence is simulated with a better timing accuracy than in the San Joaquin Valley. The times of increasing and decreasing wind speeds during the morning and evening respectively are well simulated. However, the amplitude of the maximum wind speed is overestimated so that the maximum RMSE is generally found at the time of maximum wind speed. Most days, the land breeze is weak with only a few hourly measurements indicative of an easterly wind. WRF generally overestimates the strength of the land breeze.

Other factors can explain the discrepancies between WRF and station temperatures. The WRF values used for the comparison with the stations data actually correspond to the stations' closest grid points. The spatial resolution of the simulation is 4km so the largest possible distance between a CIMIS station and its corresponding WRF grid point is 2.8km. In a complex terrain, this distance can be translated into an elevation error of a few to hundreds of meters. This can add up to the inherent topography error in WRF and increase the temperature errors. Also, different proximities to the hills lead to a different channeling of the wind.

Overall, the simulated times of minimum and maximum temperatures are very close to the observations but WRF showed a warm bias over most of the stations and most of the times. On average, WRF has a higher error during the evening that can be related with the simulation of the sea breeze that is overestimated in its evening part.

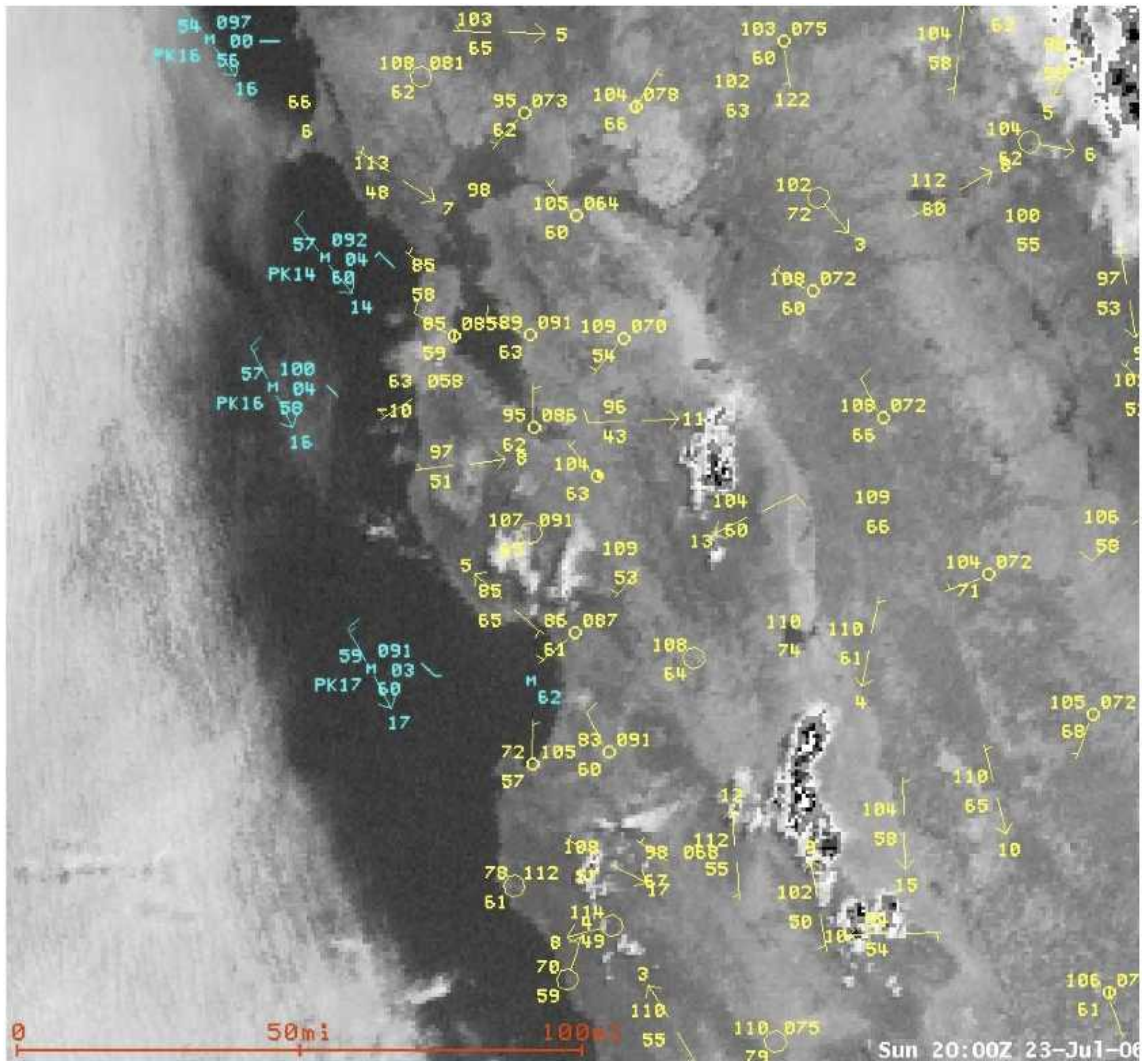


Figure 16: from (Blier, 2007), VIS satellite image of the Central California Coast at 2015UTC 23 July 2006 with selected 2000UTC surface (yellow) and buoys (blue) observations. A 100-mi (161 km) distance scale is indicated.

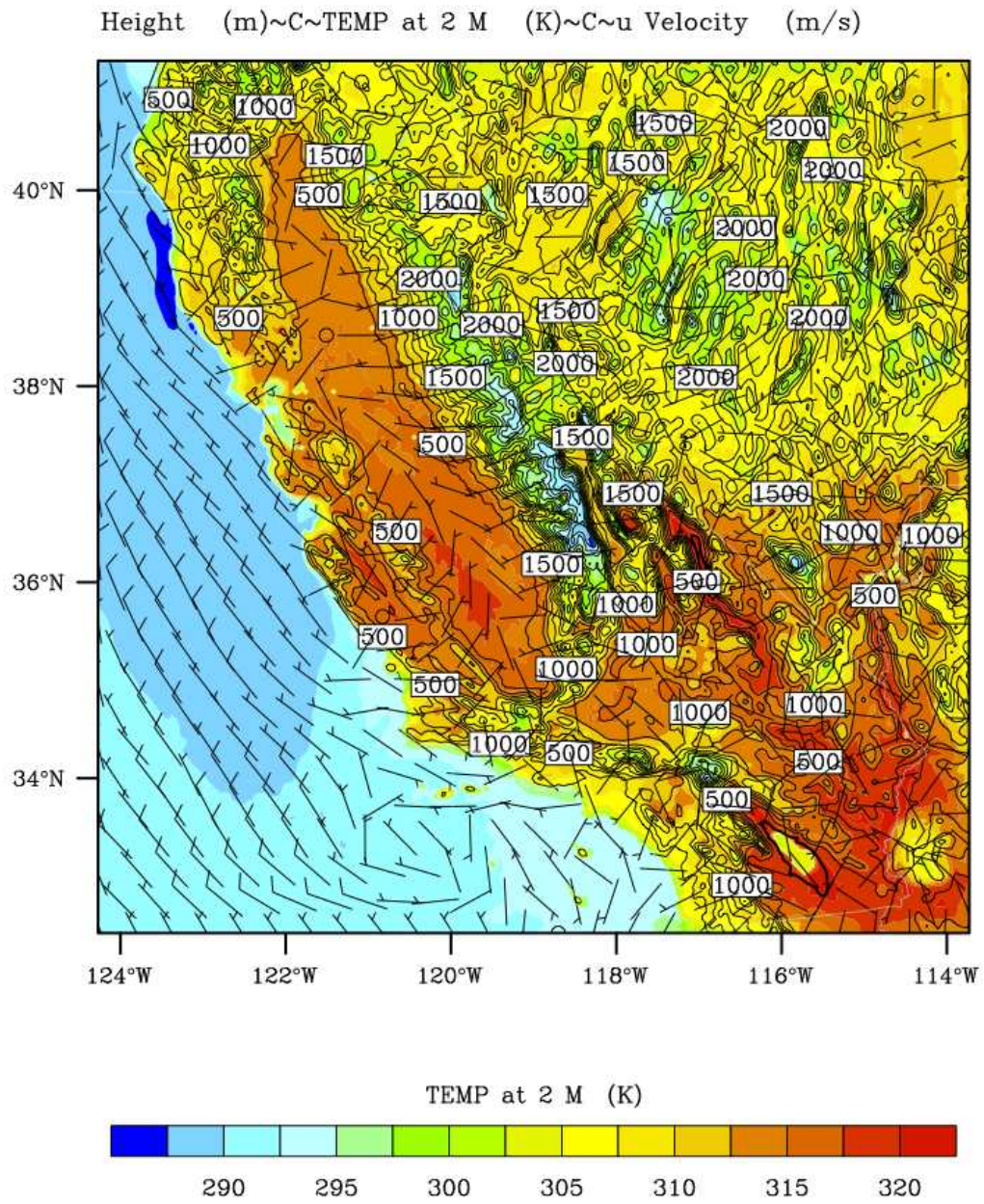


Figure 17: Wind field simulated by WRF, valid 23 July 2006, 2000UTC.

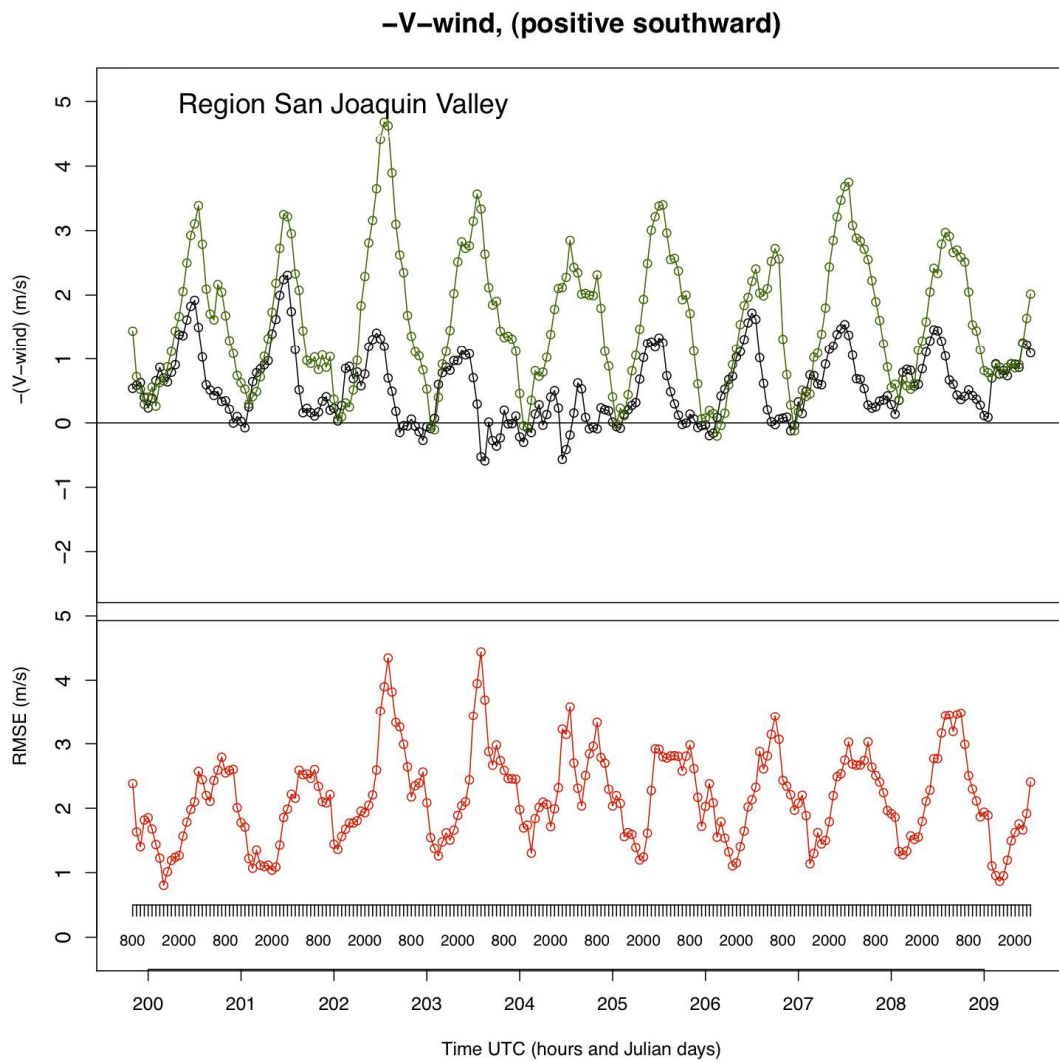


Figure 18: Comparison of WRF and CIMIS meridional wind components (-V plotted such as to have a positive southward wind). In black: hourly CIMIS observations; in green: WRF simulations; in red: RMSE. Averages for all the stations within the Central Coast Valleys region

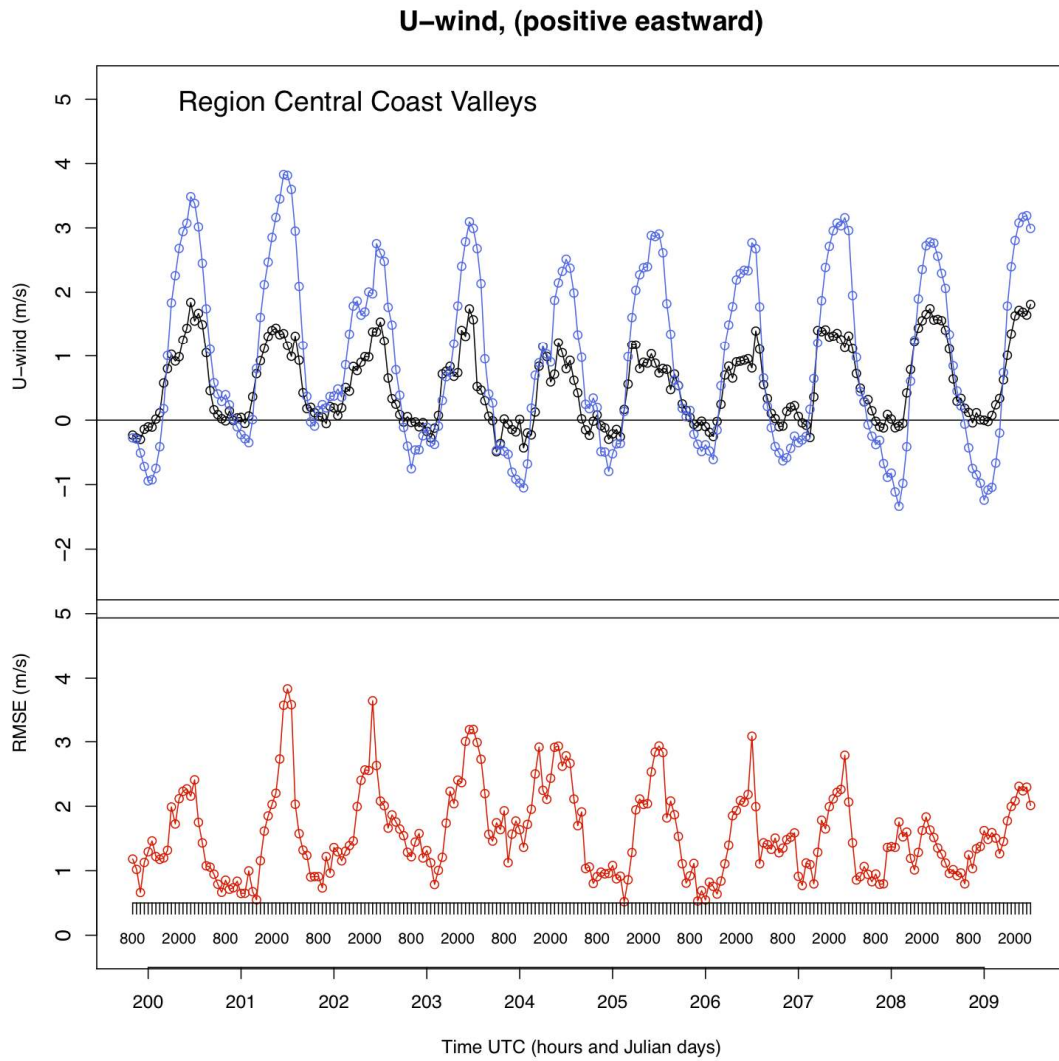


Figure 19: Comparison of WRF and CIMIS zonal wind components (U wind). In black: hourly CIMIS observations; in green: WRF simulations; in red: RMSE. Averages for all the stations within the Central Coast Valleys region

4.2. Spatial distribution of the temperature field: Simulation of Skin temperature

Previous studies (Jin et al., 1997) emphasize the importance of the accuracy of the simulation of skin temperature by a model, arguing that its diurnal variations bond air temperature and land processes together. Thus, how well a model can simulate skin temperature is a good diagnosis of the model simulation of physical processes related to the surface energy balance and exchanges between the atmosphere and the surface.

The availability of satellite retrievals of skin temperature allows an analysis of the bias of the simulation on a statewide scale. The skin temperature simulated by WRF is compared with the observations from MODIS. For this, the MODIS data are first regridded onto the WRF grid using a nearest-neighbor method (NCAR Command Language, NCL function `triple2grid`). The difference WRF-MODIS is then calculated and plotted (Figure 23).

The error patterns are very consistent between retrievals of the same hour on different days, suggesting that a large component of the bias is systematic and related to a static field. Further investigation reveals that if the temperature bias patterns show similarities with the topographical features, their contours match even more the land cover distribution. Indeed the contours of the land cover categories plotted in black on Figure 20 are similar to the T_{skin} error patterns represented in color shades (orange for warm bias and blue for cold bias). The relation between land cover and the accuracy of the mesoscale models has been evaluated in particular cases such as a regional study in Turkey (Sertel et al., 2009). It was found that the land cover dataset used by

WRF are out of date and include misclassifications. The comparison of the same regional numerical experiment with the WRF land cover dataset (USGS) versus with a new updated land cover dataset shows that surface air temperature and especially the daily maximum temperature are sensitive to the quality of the land cover parameterization. Improving the quality of the land cover leads to a diminution of the root mean square error. Examples of relation between land cover and temperature are described based on land use change. Changes in land use from croplands to urban, from forest to urban, or from woodlands to urban were found to cause regional warming through an increase in albedo, roughness length and stomatal resistance (Sertel et al., 2009).

2006-07-25 0615 : WRF - MODIS

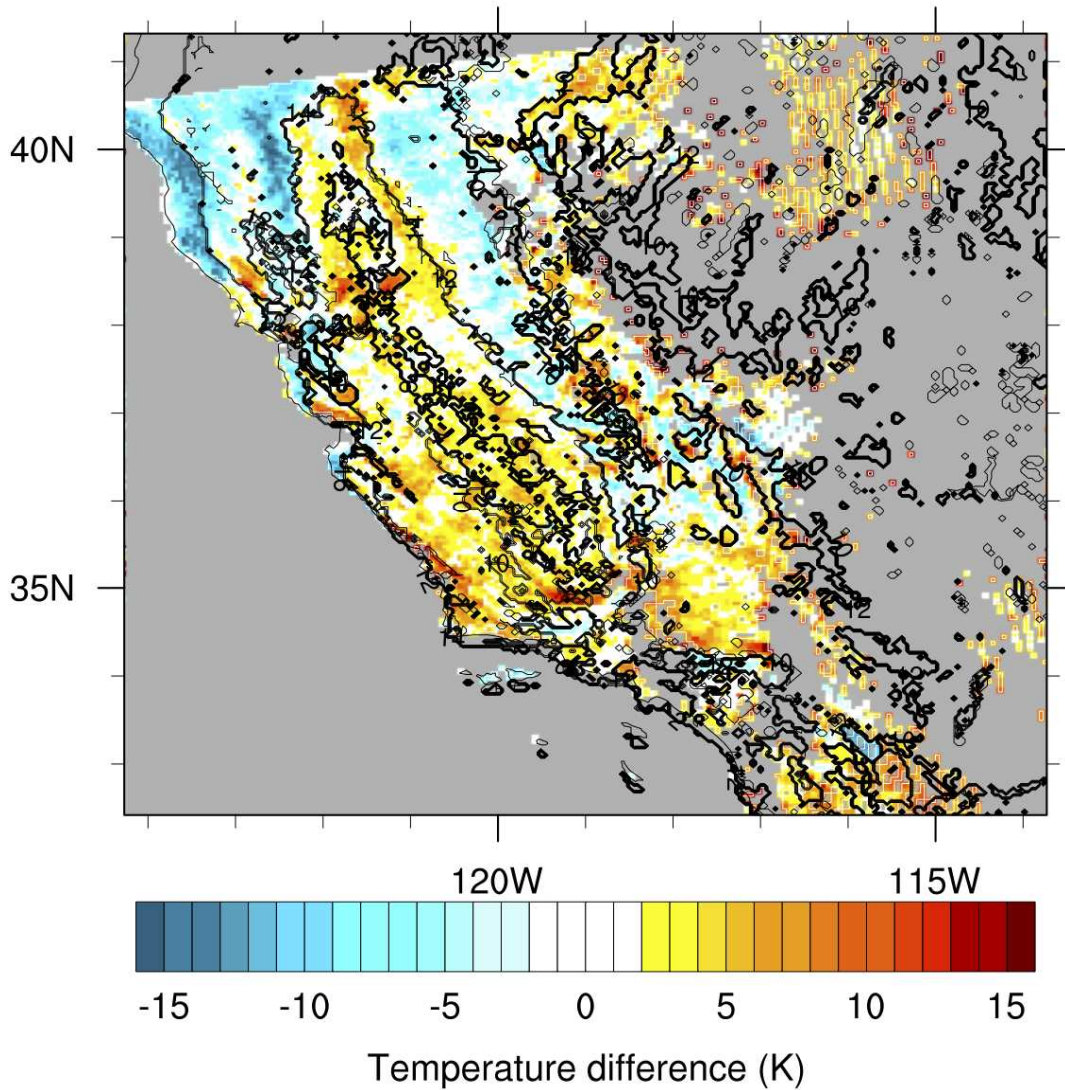
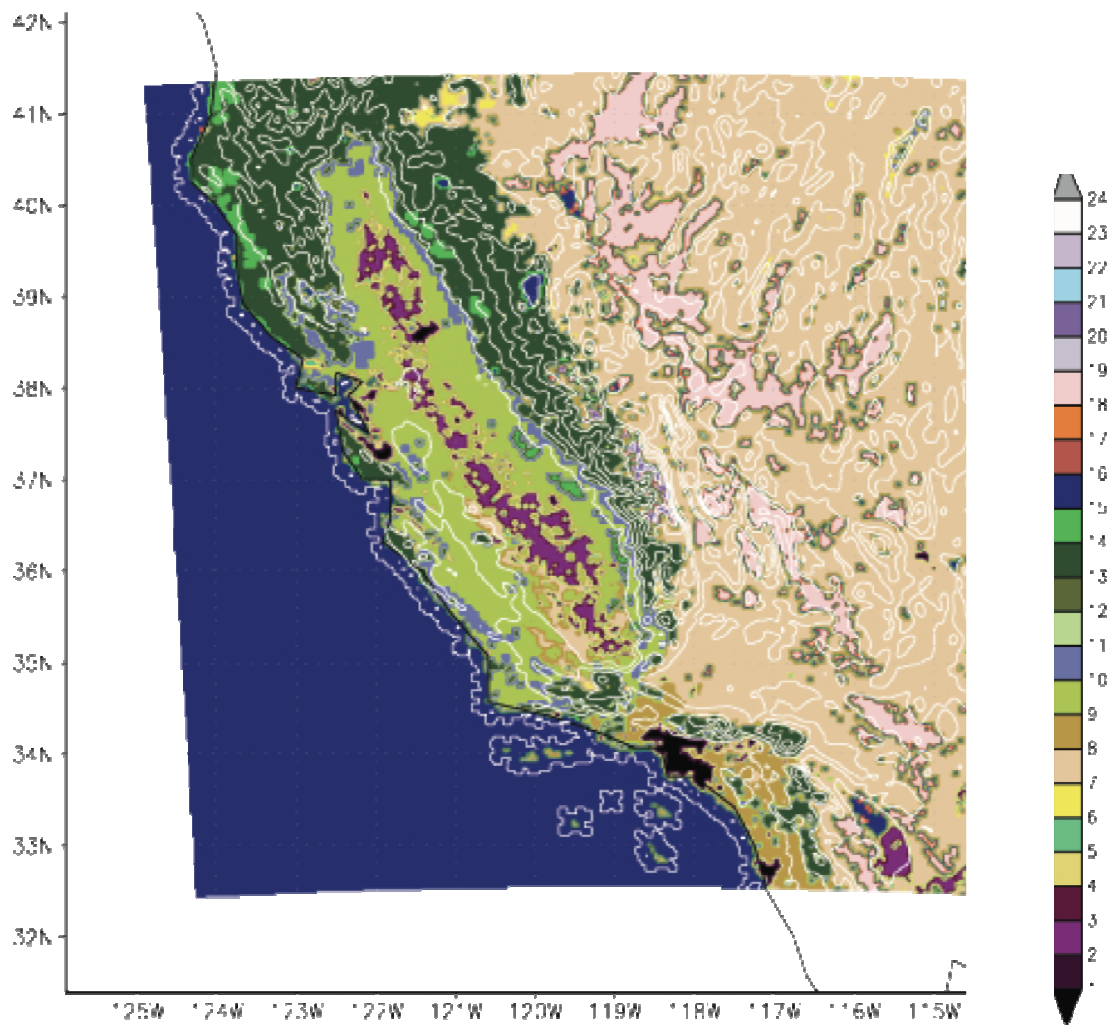


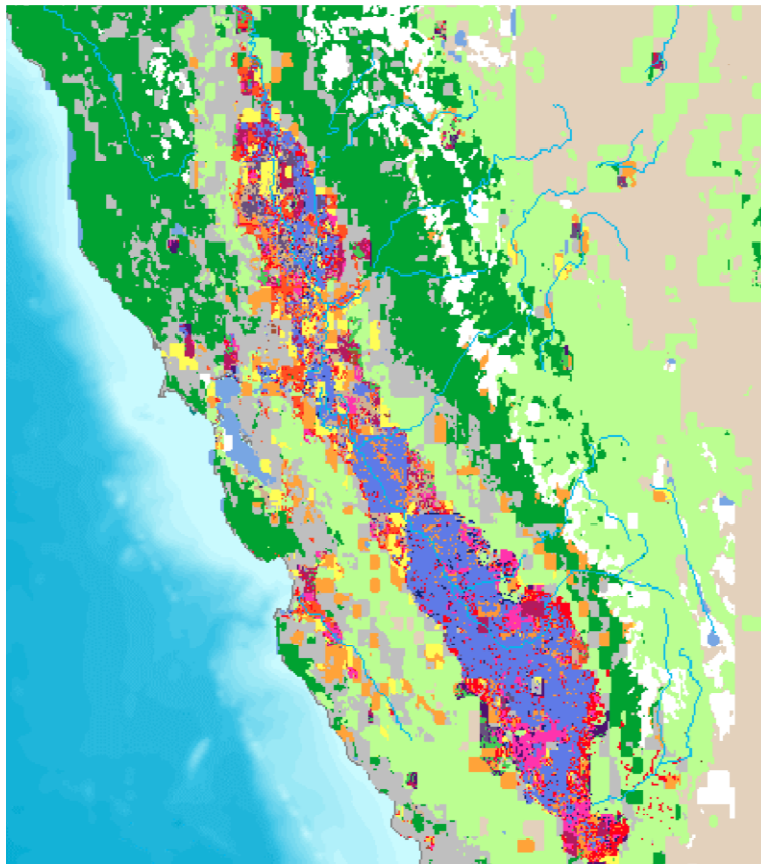
Figure 20: Comparison of the patterns in the WRF-MODIS difference and the land cover. Figure valid for July 25th, 2006 at 0615GMT. The difference between WRF and MODIS fields is represented with the filled colors and the land cover categories are overlaid with black contours



24	Snow/ice	12	Deciduous needleleaf forest
23	Bare ground tundra	11	Deciduous broadleaf forest
22	Mixed tundra	10	Savanna
21	Wooded tundra	9	Mixed shrubland/grassland
20	Herbaceous tundra	8	Shrubland
19	Barren or sparsely vegetated	7	Grassland
18	Wooden wetland	6	Cropland/woodland mosaic
17	Herbaceous wetland	5	Cropland/grassland mosaic
16	Water bodies	4	Mixed dryland/irrig. cropland
15	Mixed forest	3	Irrigated cropland and
14	Evergreen needleleaf	2	Dryland cropland and pasture
13	Evergreen broadleaf	1	Urban and built-up land

Figure 21: USGS Land cover categories developed for global purposes (colors) and wrf topography contours (white contours).

b


Global Irrigated Area

01	Irrigated, surface water, single crop, wheat-corn-cotton
02	Irrigated, surface water, single crop, cotton-rice-wheat
03	Irrigated, surface water, single crop, mixed-crops
04	Irrigated, surface water, double crop, rice-wheat-cotton
05	Irrigated, surface water, double crop, rice-wheat-cotton-corn
06	Irrigated, surface water, double crop, rice-wheat-plantations
07	Irrigated, surface water, double crop, sugarcane
08	Irrigated, surface water, double crop, mixed-crops
09	Irrigated, surface water, continuous crop, sugarcane
10	Irrigated, surface water, continuous crop, plantations
18	Irrigated, conjunctive use, single crop, corn-soybeans-other crops
19	Irrigated, conjunctive use, single crop, pastures
20	Irrigated, conjunctive use, single crop, pasture, wheat, sugarcane
21	Irrigated, conjunctive use, single crop, mixed-crops
22	Irrigated, conjunctive use, double crop, rice-wheat-sugarcane
23	Irrigated, conjunctive use, double crop, sugarcane-other crops
24	Irrigated, conjunctive use, double crop, mixed-crops
25	Irrigated, conjunctive use, continuous crop, rice-wheat
26	Irrigated, conjunctive use, continuous crop, rice-wheat-corn
27	Irrigated, conjunctive use, continuous crop, sugarcane-orchards-rice
28	Irrigated, conjunctive use, continuous crop, mixed-crops

Global LULC

00	Background
01	Irrigated, surface water
02	Irrigated, ground water / conjunctive use
03	Rainfed croplands
04	Rainfed croplands and grasslands/shrublands
05	Natural vegetation with rainfed fragments
06	Forests
07	Savanna: grasslands, shrublands
08	Barren lands, deserts or sparse vegetation
09	Snow, ice, tundra
10	Water body

Figure 22: (b) California irrigated areas (Thenkabail et al., 2009)

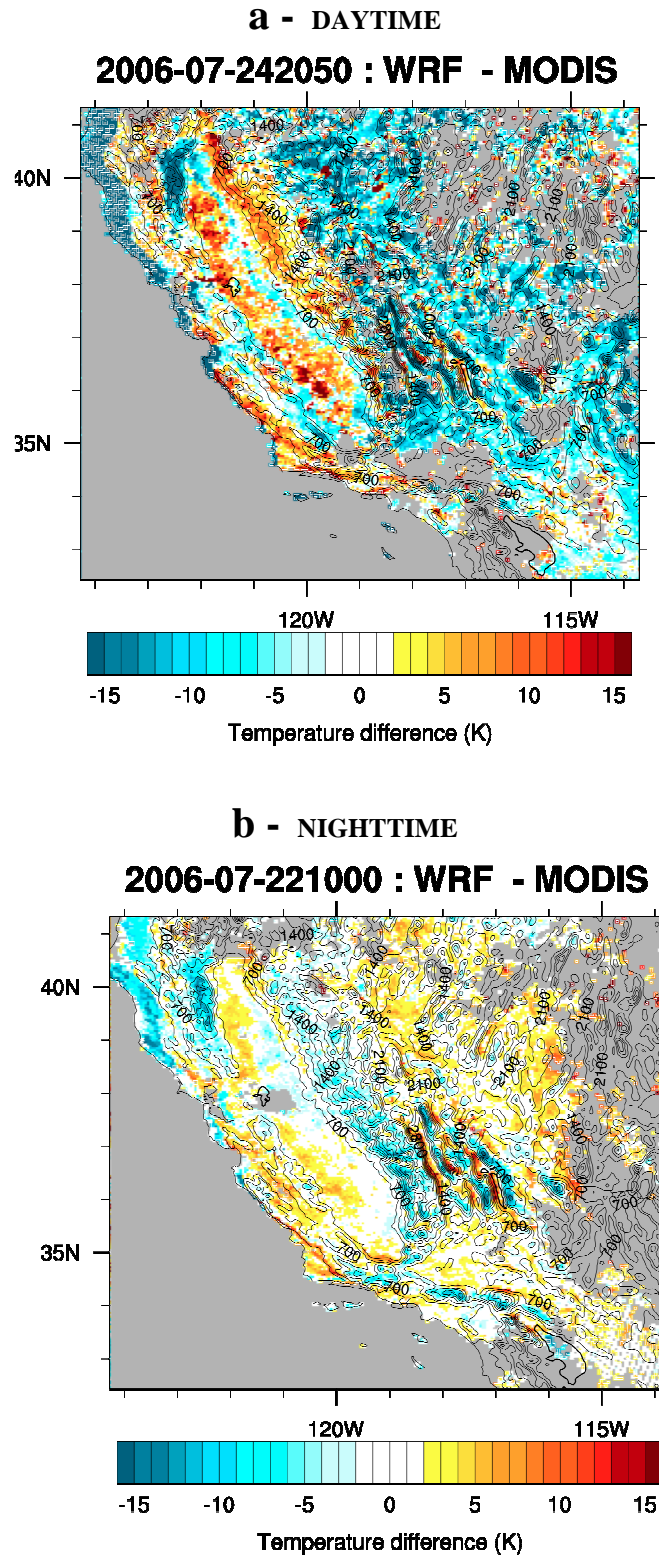


Figure 23: Typical patterns for WRF-MODIS error (color scale) and WRF elevation (contours).
 (a) daytime example (valid July 24th, 2006, 2050GMT, 1350LT)
 (b) nighttime example (valid July 22nd, 2006, 1000GMT, 700LT)

The areas where the bias is the largest are approximately the same during the day and at night but the sign of the bias can vary from one to the other. These patterns can be linked to the land cover.

Figure 22 (a) (Easter, 2004) is a high-resolution representation of the various types of vegetation found in California. The land cover used for the parameterization of WRF is the widely used 24-category land use USGS dataset (Loveland et al., 1995) that has been developed for global scale purposes. The USGS Land use dataset has been derived from April 1992 to March 1993 AVHRR observations and has a 30second resolution (approximately 1km). The WRF Preprocessing program metgrid is used to interpolate these data to the WRF grid, at 4km resolution in this study.

For this discussion, the USGS land cover used by WRF is used along with the vegetation characterization from Easter 2004 (E2004) (Figure22(a) and a map of the irrigation patterns in California (Thenkabail et al. (2009),Figure 22(b)).

Figure 22(a) is more recent, and includes local species instead of only land cover types as in the USGS dataset (USGS) suitable for global classification. Figure 22 (b) is a map of the irrigated areas in the Central Valley and gives more details about the distribution of the irrigation patterns in the Central Valley.

In some areas, the sign of the WRF skin temperature bias is the same at day and at night but larger at day. This is the case in the Central Valley, along a portion of the Pacific coast and in the Basin and Range province.

The central portion of the San Joaquin Valley and Sacramento Valley is primarily irrigated agriculture (dark pink on Figure 22(a)). Between the irrigated valley bottom and the woodlands of the Sierra Foothills lie non-irrigated grasslands classified as savanna by the USGS. The savanna areas are consistently found to be colder in WRF than in the observations. Around the savanna areas, including the lower Sierra

Foothills, the main landcover consists of oak woodland and is categorized as deciduous broadleaf forest in USGS. The temperature in the irrigated areas (Figure 22) in the center of the Valley as well as in the oak woodlands near the Sierra Foothills is simulated with a constant warm bias (larger bias during daytime than nighttime). The area covered by irrigated agriculture and grassland is different in both datasets and might cause some of the bias. The more recent and more detailed E2004 (Figure 22) shows a larger agricultural area than is classified as such in USGS, probably as a consequence of land use change between the early 90s (creation of the USGS dataset) and early 2000 (E2004).

Along the Central Coast, between the Monterey Bay and the Santa Barbara area, along the Santa Lucia range of coastal mountains, the vegetation consists of a mix of natural forests with mainly coniferous in the north (evergreen needleleaf in USGS), chaparral in the center (savanna and deciduous broadleaf in USGS) and oak woodland and grassland in the south (deciduous broadleaf in USGS). The temperature in these coastal areas is too warm in the WRF simulations both at day and night.

The south half of the Sierra Nevada includes the highest elevations of the state and consists of deep valleys with rivers going down to the San Joaquin Valley and high elevations both covered with 'evergreen needleleaf' species in USGS. The valleys are simulated as too warm as opposed to the rest of the range where the WRF temperature is colder than in MODIS. A reason for this can be related to the difference in the resolution of MODIS and WRF. MODIS observations are retrieved at 1km horizontal resolution, whereas WRF is run at 4km resolution. In the case of very steep valleys where each kilometer represents an important change in elevation, such a difference in resolution might cause consistent discrepancies in the topography resolved and therefore in the associated temperature field.

The Basin and Range province lies east of the Sierra Nevada. This arid area consists of mountain ranges, basins and deserts. In California, it includes high peaks (Waucoba Mountain, Telescope Peak, both above 3000m) and low valleys (Death Valley, lowest point in the western hemisphere). The USGS land cover follows the large scale elevation contours (Figure 21) with the valleys being classified as ‘barren or sparsely vegetated’ whereas the mountains and deserts belong to the shrubland category in USGS. Here, we find the same bias as in the southwestern steep valleys of the Sierra. In this entire region, the WRF simulation of skin temperature has the same bias at night and at day: the valleys are consistently found warmer in WRF than in MODIS and the high mountain areas are colder in the WRF simulations than in the MODIS retrievals. As was suggested in the case of the south Sierra, the difference in resolution between WRF and MODIS might cause a difference in the accuracy of the topography resulting in a constant temperature bias.

Other domains have a different bias sign depending on the time of the day.

The categories “Pacific coniferous forest” and “Lower/Upper montane” are two categories of evergreen needleleaves mainly found in the Sierra around the Central Valley to the East and the North (dark green and red on Figure 22(a)). Also, in Southern California, the Transverse Range East of the Los Angeles Basin is covered with a mixture of coniferous and chaparral vegetation along the range arc joining the Coast to the east of the Los Angeles basin. These species of conifers are differentiated in E2004 but not in USGS in which both of them are classified in the “evergreen needleleaf” category. All of these areas have a warm bias during the day and a cold bias during the night, amplifying the diurnal cycle of land temperature.

The landcover in the Mojave Desert, southeast of the Sierra Nevada, and south of the Basin and Range region, is defined as a mixture of shrubland and ‘barren or sparsely vegetated’ in USGS and as scrub (desert scrub and alkaline scrub) in E2004. In this area, the WRF bias of skin temperature is opposite to the one for the coniferous areas of the Sierras with a warm bias at night and cold bias during the day, yielding a reduced diurnal temperature range.

Vegetation characteristics such as the type of vegetation, its canopy water content or leaf area index are highly impacted by the water content of the soil. In turn, these land cover parameters play a role in the energy balance at the interface with the atmosphere and therefore in the partitioning of heat fluxes between latent and sensible fluxes (Hong et al., 2007) and on skin temperature. During the daytime, the exchanges of water and energy between the vegetation and the atmosphere are more important than at night. This is consistent with the larger magnitude of the bias during the day than at night. The consistency of the bias in WRF skin temperature with the land cover and irrigation patterns is investigated through its relation with soil moisture.

The soil moisture simulated by WRF is compared with outputs from the Land Information System. The Land Information System needs 24 months to reach equilibrium (method described in Appendix 4) and has therefore been run for two complete annual cycles. In both runs, the same LSM is run (Noah) at the same resolution. However, the atmospheric forcing is different: NCEP reanalyses data for LIS and coupled atmospheric simulation for WRF. Another major difference is the length of the run, at the time shown in the analysis on Figure 26 (0 GMT, July 25), the LIS has been run for two complete annual cycles (Figure 24) and has reached

equilibrium (Appendix 4). In the corresponding (Figure 25) WRF has been run for 6 days and its soil moisture field is still very close to the initial field shown in Figure 27 both in the top (b) and bottom (a) layers.

LIS has been evaluated in several studies (Case et al., 2008; Mostovoy and Anantharaj, 2007). In the absence of a regional coverage of observation data for soil data, it is here used as a comparison to evaluate WRF's simulation of the soil. An example is shown in Figure 24 and Figure 25 for soil moisture. Figure 24 and Figure 25 show the top (Figure 24(a) and Figure 25(a)) and bottom (Figure 24(b) and Figure 25(b)) layers of soil moisture (respectively 0-10cm and 100-200cm deep) calculated by WRF and LIS for 0GMT on the 25th of July 2006.

The results obtained with LIS show high-resolution features in the moisture field whereas local results are more homogeneous with WRF. Generally, the differences in soil moisture have similar features on the top and the bottom layer but are larger on the deepest layer. On the top surface layer (Figure 24(a) and Figure 25(a)), the dry areas in the south of the state are either in agreement between WRF and LIS with values around 0.06 or drier such as around the border with Arizona.

The rest of the domain is generally wetter in the WRF data. Both models find the highest soil moisture of the domain over the South Sierra but WRF finds it much wetter with peaks around 0.3 (LIS only finds values around 0.23).

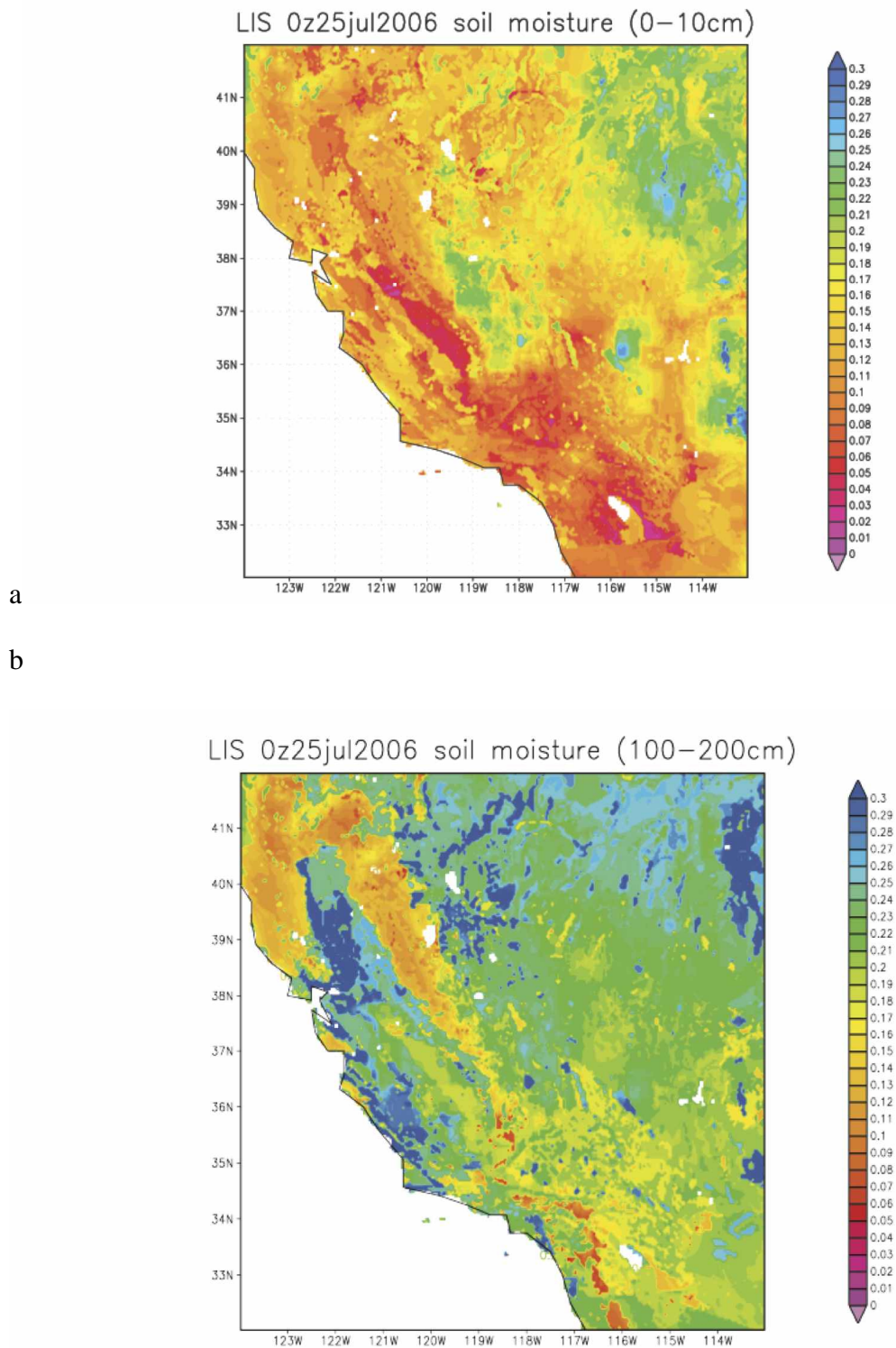
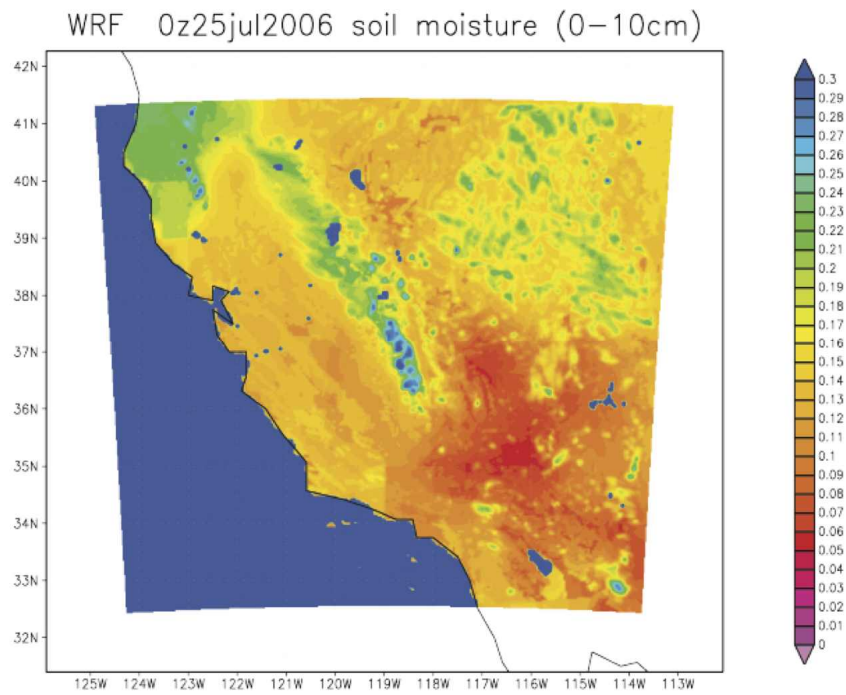


Figure 24: LIS volumetric soil moisture fields for a: layer 1 (0-10cm, top), b: layer 4 (100-200cm, bottom), valid July 25th, 2006, 00GMT.

a



b

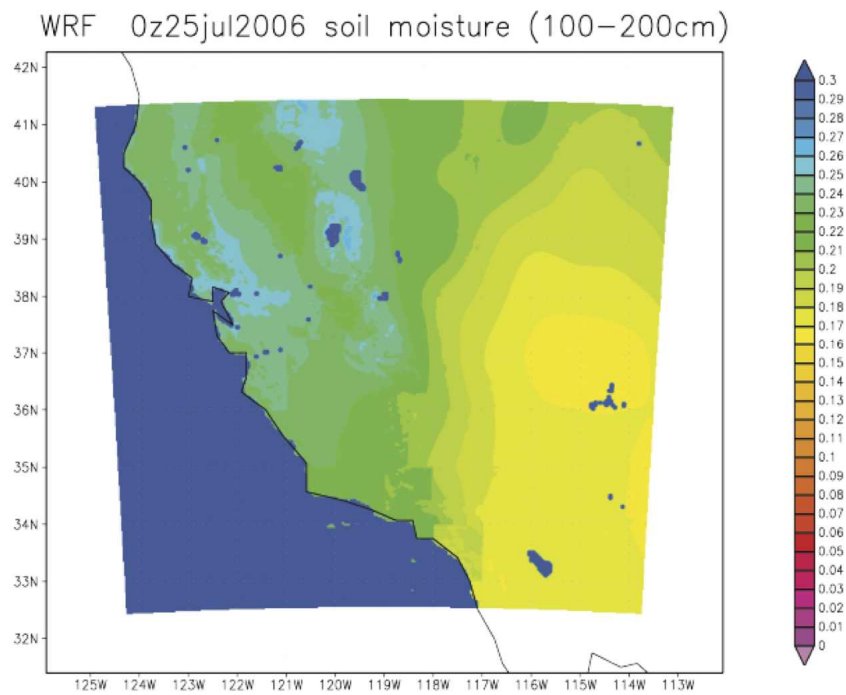
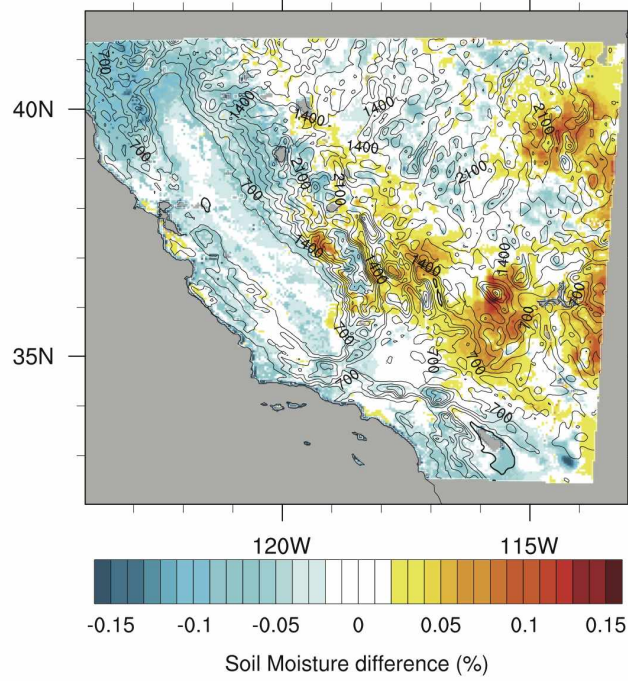


Figure 25: WRF volumetric soil moisture fields for a: layer 1 (0-10cm, top), b: layer 4 (100-200cm, bottom), valid July 25th, 2006, 00GMT.

a

2006-07-25 0000 : LIS - WRF layer 1



b

2006-07-25 0000 : LIS - WRF layer 4

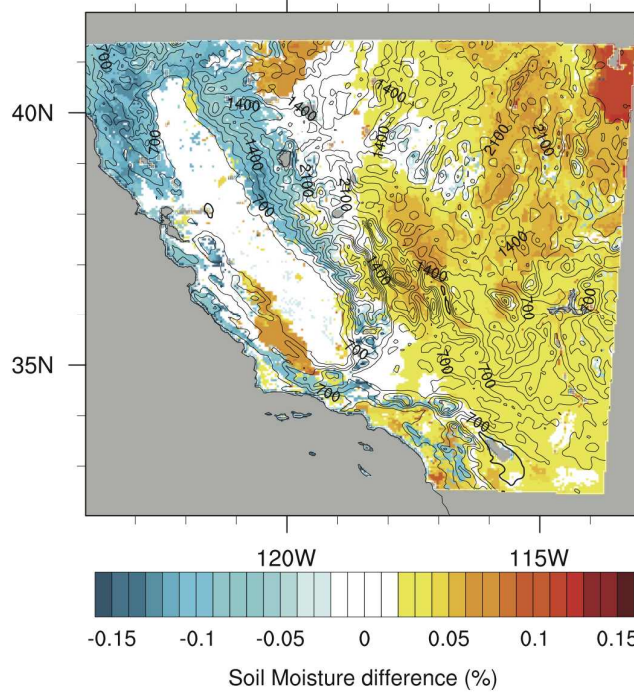


Figure 26: (LIS-WRF) volumetric soil moisture fields for a: layer 1 (0-10cm, top), b: layer 4 (100-200cm, bottom), valid July 25th, 2006, 00GMT.

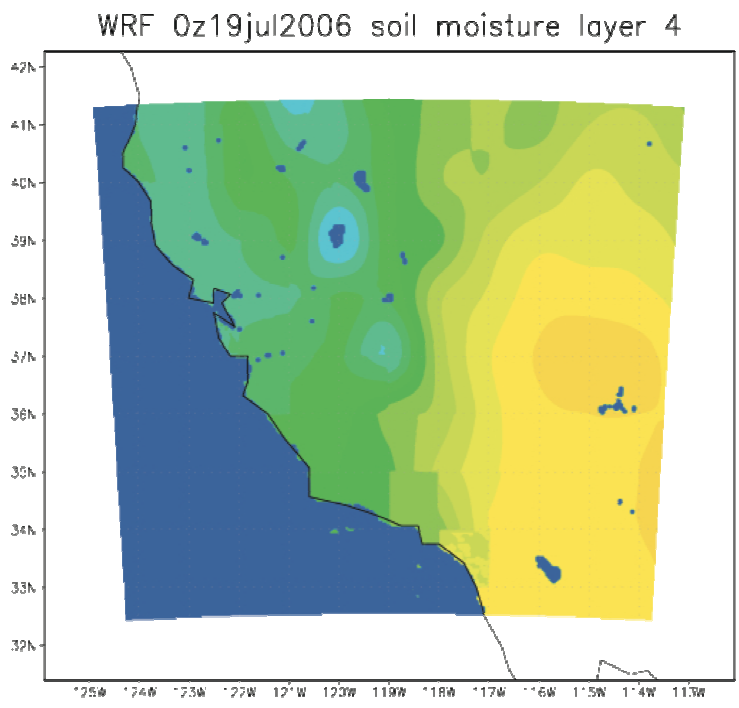
The top layer has the most influences on surface atmospheric processes. In the top layer, the main areas of disagreement between LIS and WRF (Figure 26(a)) are located in the Sierras north and east of the Central Valley, in the coniferous forest areas, where WRF finds an average value of 0.2 whereas LIS finds values around 0.12 with more local variation.

During daytime, all the areas where the soil moisture is larger in WRF than in LIS have a warm skin temperature bias, such as the mountain ranges north and east of the Central Valley or the Central Coast and transverse ranges. At night, the relation between soil moisture and skin temperature bias is not as clear. Mountainous areas such as the Sierra Nevada or the Transverse ranges have a cold error whereas the temperatures in the Central Coast region are warmer in WRF than in the MODIS observations.

Only few areas in California are found to have lower soil moisture in the WRF than in LIS simulations. All of these areas are located in the southeastern deserts and their temperature simulations yield a cold bias of WRF during the day and warm at night. Several reasons have been suggested for the spatial distribution of the errors in the WRF simulation of skin temperature, such as misclassification.

Misclassification can either be due to land use change since the creation of the dataset or to a lack of species differentiation. An example of land use change is in the Central Valley where the agricultural irrigated areas have extended around the central axis of the Central Valley. This type of underestimation of irrigation yields to a cold bias in the simulation of skin temperature. The urban areas are also smaller in the USGS dataset than in the more recent E2004. A lack of differentiation resulting in misclassification seems to occur in the Central Coast areas.

a



b

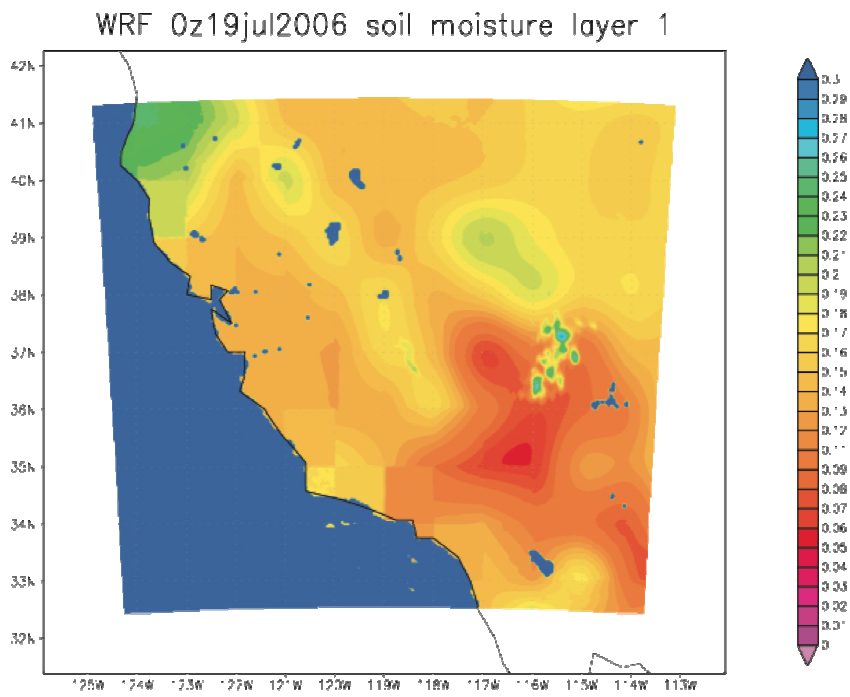


Figure 27: Initial soil moisture conditions for WRF (cm3/cm3) for the deepest layer (layer 4 (a)) and the top layer (layer 1 (b))

Where USGS only finds uniform areas of ‘evergreen needleleaves’, savanna, and oak woodlands, E2004 describes a complex mixture of conifers, oak woodland, grassland and also includes an area of agricultural land cover south of Monterey that is not differentiated by USGS. The classification of all these species as savanna, area yields to temperature biases: conifers classified as savanna yield a cold bias, and agricultural, grassland, oak woodland, areas, misclassified as savanna yield a warm bias. Soil moisture, especially in the bottom layer, also seems related to the error patterns in this region. Along the coast, a band with a large wet error also has a warm temperature bias. East of this band, another area with a strong dry error has a cold bias during the day and a warm bias at night. Only three areas are found to have a dry bias in the bottom layer (Central Coast Valleys west of the San Joaquin Valley; the Los Angeles Basin, between the Transverse Range and the coast; and the Basin and Range province, east of the Sierra Nevada). In these three areas, WRF simulation of skin temperature is colder during the day and warmer during the night than the MODIS measurements.

The difference in resolution between WRF and MODIS can also explain some of the bias on Figure 23 such as for the steep valleys and peaks southeast of the Sierra Nevada. In this region, the difference in the ability of WRF and MODIS to capture the fast-varying topography results in a warm bias in the valleys and a cold bias at the peaks.

4.3. Relationship between Skin and Air temperature

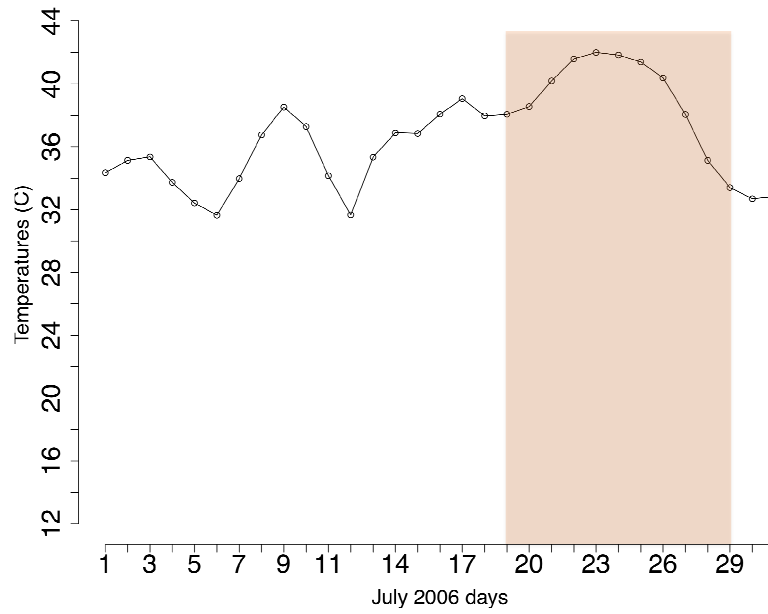
The standard surface air temperature, T_a as defined by the World Meteorological Organization (WMO) is measured by thermometers located approximately 2m above

the ground, sheltered from the direct solar radiation (so that the internal heat capacity of the sensor does not affect the measurement). It therefore represents the temperature of a thick layer of relatively homogeneous air. The skin temperature measured by satellites is derived from the radiance emitted by the surface and received by the sensor in various wavelengths. Indeed, the Stefan-Boltzmann law relating radiance and temperature for a black body has to be modified for real materials by including their emissivity. Thus, the “skin temperature” or “land surface temperature” refers to the temperature of the thin layer of the Earth that is visible to the satellite and which corresponds to the penetration depth of the electromagnetic radiation used to measure it ((Norman and Becker, 1995). This surface layer is considered infinitesimally thin, with no heat capacity, and therefore responds more quickly to changes in the local balance of energy than air temperature (Prigent et al., 2003). Thus, skin temperature is largely related to net radiation, land cover, soil’s moisture and to the processes taking place at the land-atmosphere interface.

The difference between T_{skin} and T_a is important because it drives the sensible heat flux at the land surface (Zaitchik et al., 2006). To investigate the relation between T_{skin} and T_a , two regions with different characteristics are analyzed in parallel: the San Joaquin Valley region and the Central Coast Valleys region defined in section 3.1.

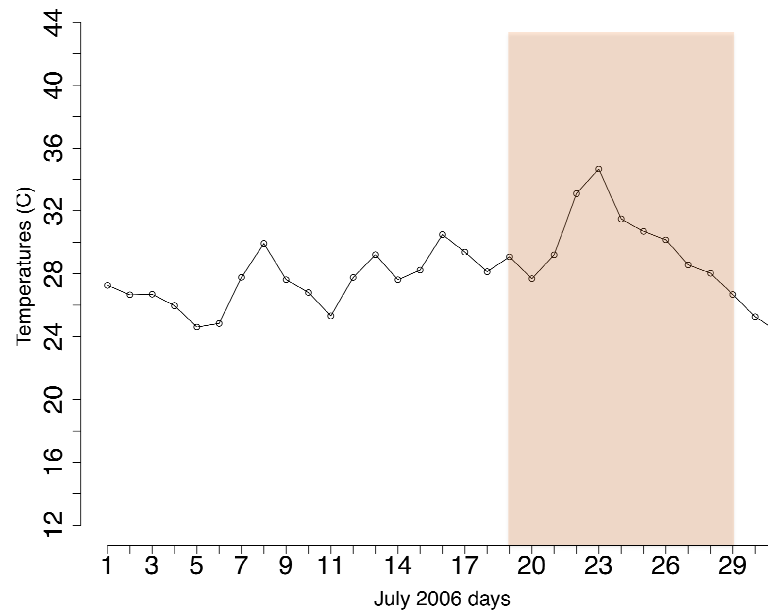
The role of wind circulation on air temperature is investigated first before focusing on the relationship between air (measured at the CIMIS stations) and skin (retrieved by the MODIS sensor) temperatures, in particular through net radiation (calculated at the CIMIS meteorological stations by a balance between incoming and outgoing radiant energy).

Daily maximum temperatures – July 2006 – San Joaquin Valley



a

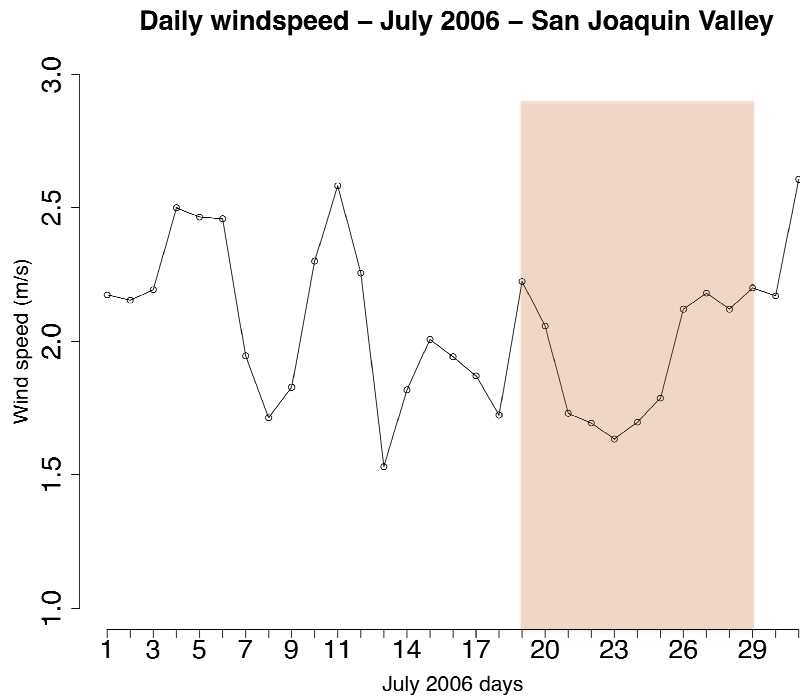
Daily maximum temperatures – July 2006 – Central Coast Valley:



b

Figure 28: Daily maximum temperatures in C, a: for the San Joaquin Valley, b: for the Central Coast valleys. The heat wave period is shown in the orange bar.

a



b

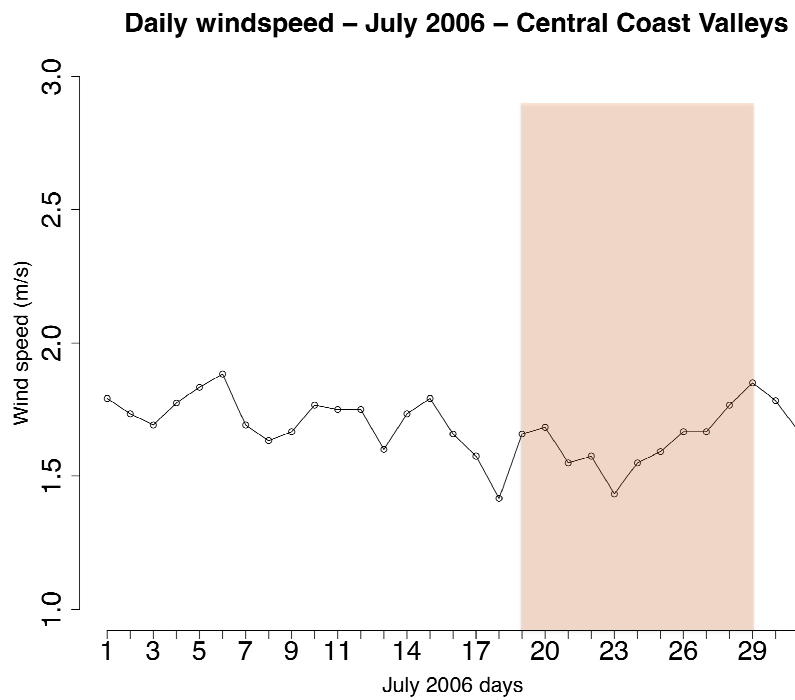
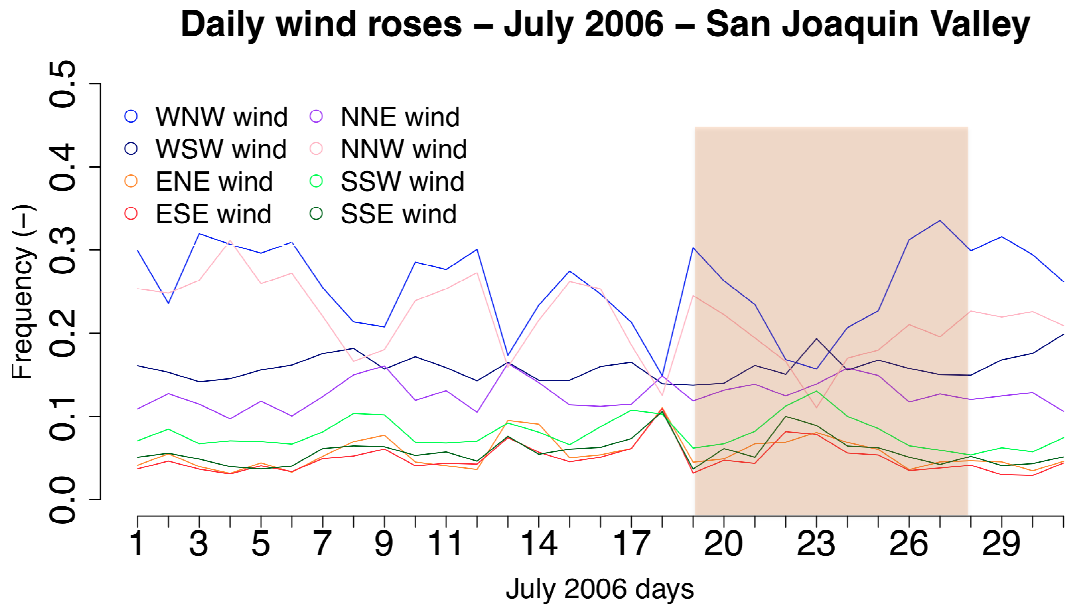


Figure 29: Daily windspeed in C, a: for the San Joaquin Valley, b: for the Central Coast valleys.

The heat wave period is shown in the orange bar.

a



b

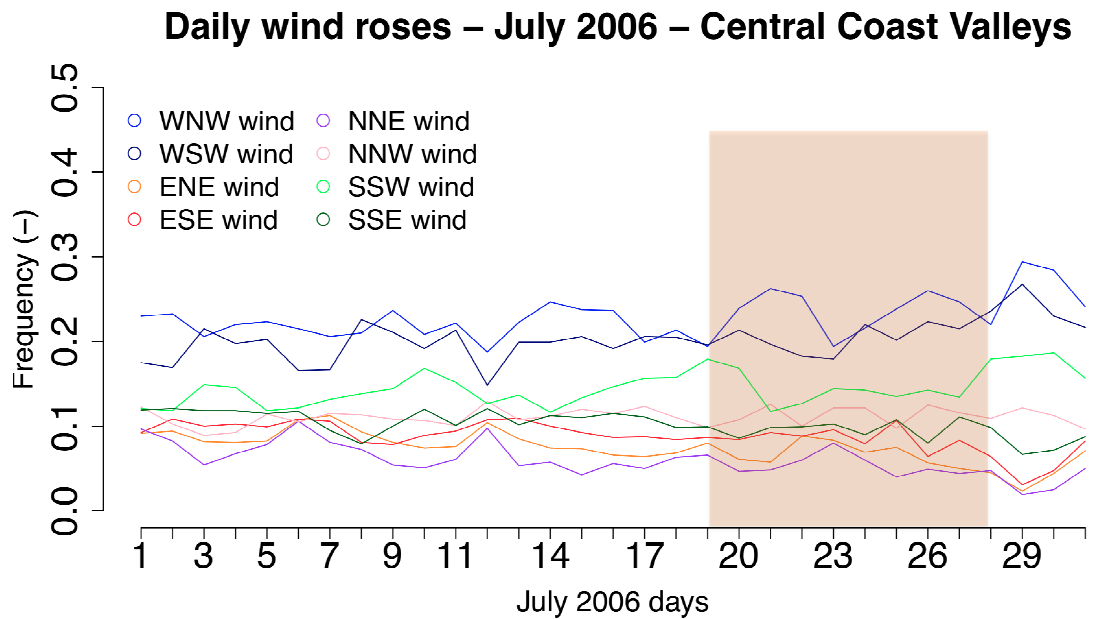


Figure 30: Daily wind roses in C, a: for the San Joaquin Valley, b: for the Central Coast valleys. The heat wave period is shown in the orange bar.

Because of the high heat capacity of the ocean, the surface marine boundary has a weak diurnal cycle of temperatures. When the wind is not offshore, the surface marine boundary layer in the coastal areas is affected by this property and tends to have a smaller diurnal temperature range. Figure 28 to Figure 30 show the time series of daily maximum air temperature, wind speed and wind directions frequencies averaged over the stations of the two regions of the San Joaquin Valley and the Central Coast Valleys for the days of July 2006. The frequencies of the wind directions are grouped into eight bins (sectors). The eight reference bins are ENE, NNE, NNW, WNW, WSW, SSW, SSE, ESE, (CIMIS website). On all of the figures, the 10-day study period centered on the peak of the heat wave is highlighted in orange.

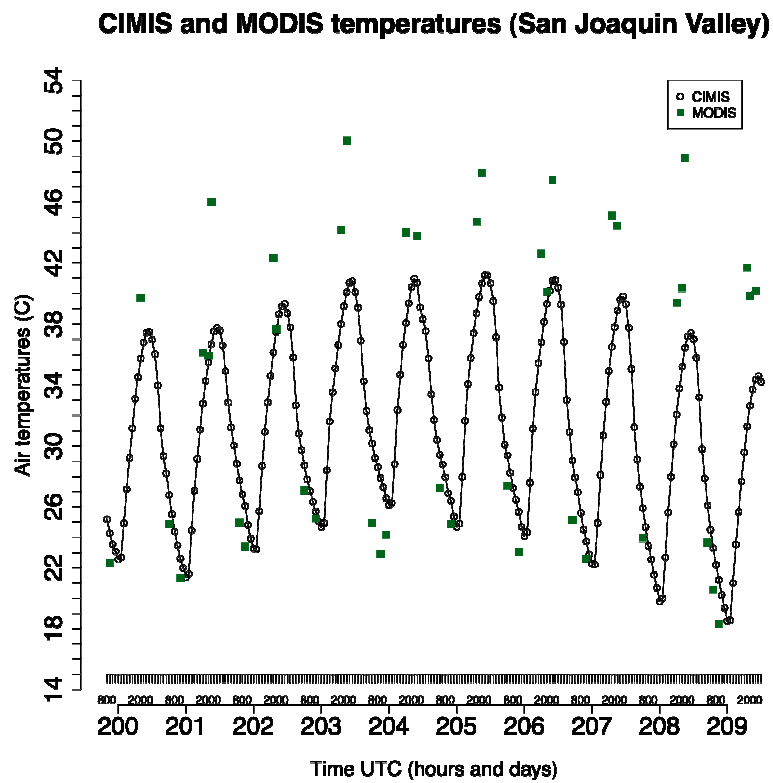
First, both regions exhibit a direct relation between air temperature and wind speed. Comparing Figure 28(a) and Figure 29(a) and for the San Joaquin Valley or Figure 28(b) and Figure 29(b) for the Central Coast Valleys, we can see that local maxima (resp. minima) in daily maximum temperatures occur for local minima (resp. maxima) wind speed. For example, between the 6th and the 11th of July the average daily maximum temperature in the Central Coast Valley regions increases from 24.8C to 29.9C (reached on the 8th) and then decreases back to 25.3C on the 11th. During the same laps of time, the average wind speed over the region decreases from 1.88m/s to 1.63m/s (reached on the 8th of July) and increases back to 1.75m/s. Similar patterns can be found for the San Joaquin Valley charts. It is noteworthy that this is also true during the heat wave highlighted in orange in Figure 28, Figure 29 and Figure 30. In both regions the very high air temperatures reached during the heat wave (42.0C in the San Joaquin Valley and 34.7C in the Central Coast Valleys) are both associated with periods of low wind speeds (1.63m/s in the San Joaquin Valley and 1.43m/s in the Central Coast Valleys).

Two differences however exist between the wind speed-air temperature relations for both regions.

First, in the San Joaquin Valley, high (low) daily maximum temperatures are associated with low (high) wind speeds but a lag of one to two days exists between the temperature maximum (minimum) and the wind speed minimum (maximum). Second, the increases and decreases in wind speed and daily maximum air temperatures have higher amplitude in the San Joaquin Valley than in the Central Coast Valleys. These two observations are illustrated with the same high temperature event used above for the Central Coast Valleys. In the Central Coast Valleys region, a drop of 0.25m/s in the wind speed yields an increase in daily maximum temperature of 5.1C. In the San Joaquin Valley, during the same event, a decrease of 0.73m/s in the wind speed results in an increase in the daily maximum temperature of 6.9C. In the Central Coast Valleys, small variations in the wind speed are sufficient to affect the daily maximum temperatures.

The wind direction also has a stronger variability in the San Joaquin Valley than in the Central Coast Valleys. In the San Joaquin Valley, the variations in the wind speed are closely associated with the frequency of the northwesterly winds (classified within the bins NNW and WNW). This highlights the fact that the wind in the San Joaquin Valley is channeled from the San Francisco Bay area down the valley and that the wind in the Valley is therefore highly dominated by a northwestern flow. Because of this channeling of the flow, weak winds cannot reach the San Joaquin Valley, consistent with the stronger variability in the wind speed in the San Joaquin Valley than in the coastal areas directly exposed to the marine air.

a



b

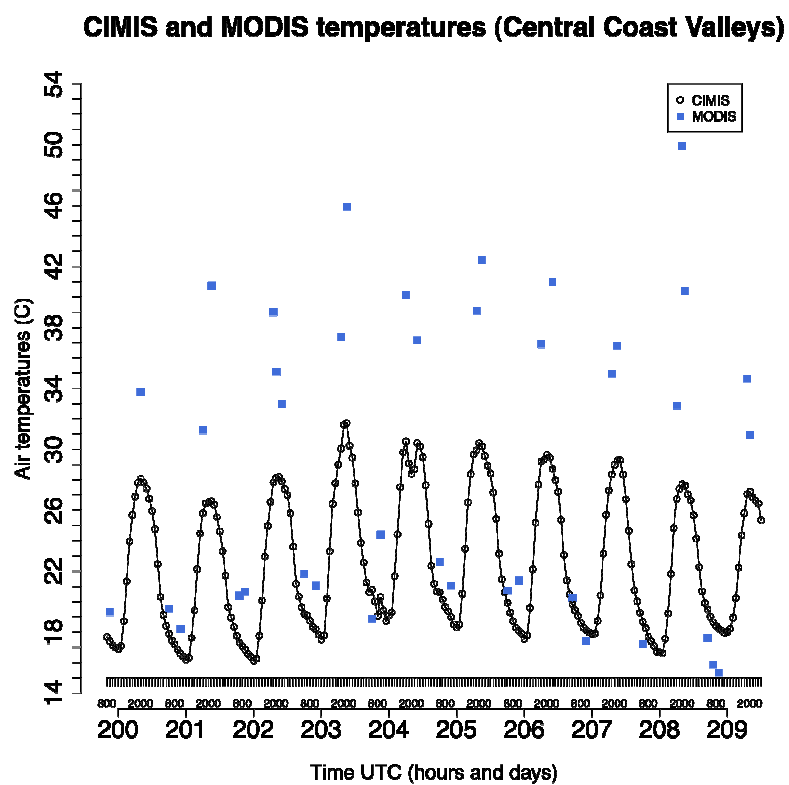
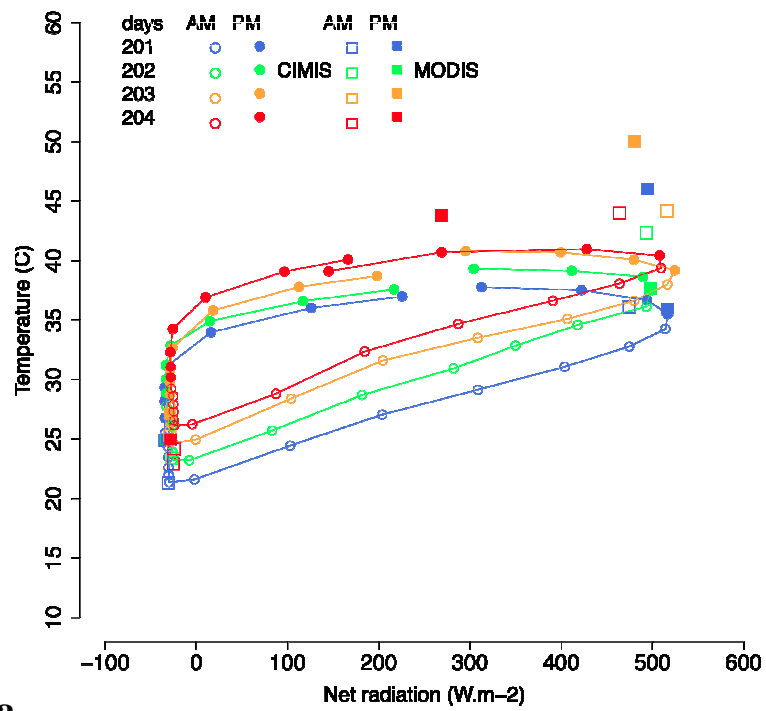


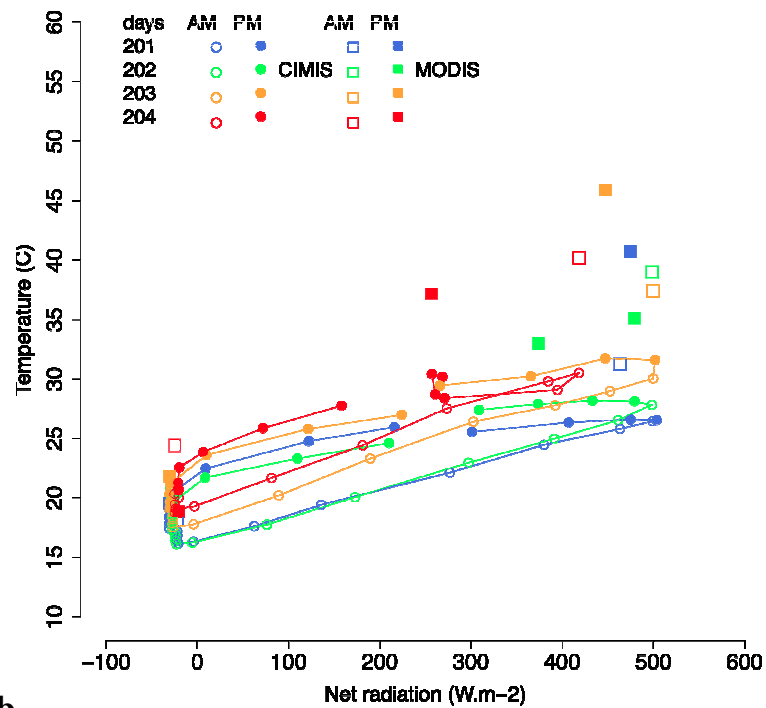
Figure 31: Comparison of MODIS and CIMIS observed temperatures averaged over the stations of the climate regions of the Central Valley as a function of time, a: for the regions San Joaquin valley, b: Central Coast Valleys.

Temperature vs Radiation cycle (San Joaquin Valley)



a

Temperature vs Radiation cycle (Central Coast Valleys)



b

Figure 32: Comparison of MODIS and CIMIS observed temperatures averaged over the stations of the climate regions of the Central Valley as a function of time, a: for the regions San Joaquin valley, b: Central Coast Valleys.

Figure 31 and Figure 32 investigate the relation between T_{skin} and T_a . The MODIS retrievals are interpolated to the exact stations locations using an inverse-distance weighted average over the four nearest pixels. The time series of air temperature (hourly measured by the CIMIS stations) and skin temperature (retrieved 4 times a day by MODIS) are then compared region by region). The times of overpass of MODIS over California are around 500—700GMT (2300-0100 LT) and 1800-2000GMT (1100-1300LT) for the Aqua platform and 900-1100GMT (200-400LT) and 2000-2200GMT (1300-1500LT) for the Terra platform. These times include passes that are close to the times of daily maximum and minimum temperatures (Figure 31) and will respectively be designated as night and day overpasses. The time plots in Figure 32 show the diurnal variations in the temperature measured by CIMIS (line) and MODIS (color points) as a function of the incoming radiation for the first days of the heat wave (growing phase, from the 19th to the 23rd of July). The hourly data are averaged over each of the two regions of study: the San Joaquin valley, (southern two thirds of the Central Valley, Figure 31(a) and Figure 32(a)) and the Central Coast Valleys (Figure 31(b) and Figure 32(b)). Since MODIS data are not retrieved exactly at the same time everyday, the hourly average can yield more than two day (night) MODIS points. Figure 31 represents the temperature against time, and Figure 32 represents the temperature against net radiation received at the surface (measured at the CIMIS stations). Figure 32 shows that, as the heat wave develops, from one day to another, the range of radiation received at the surface does not change but the whole cycle of air temperature is translated up by a few degrees. Therefore, if radiation is obviously a key parameter in the diurnal cycle of the temperatures, it is less important at the longer time scale over which the heat wave develops. The parallelism of the heating and cooling branches of the cycle implies

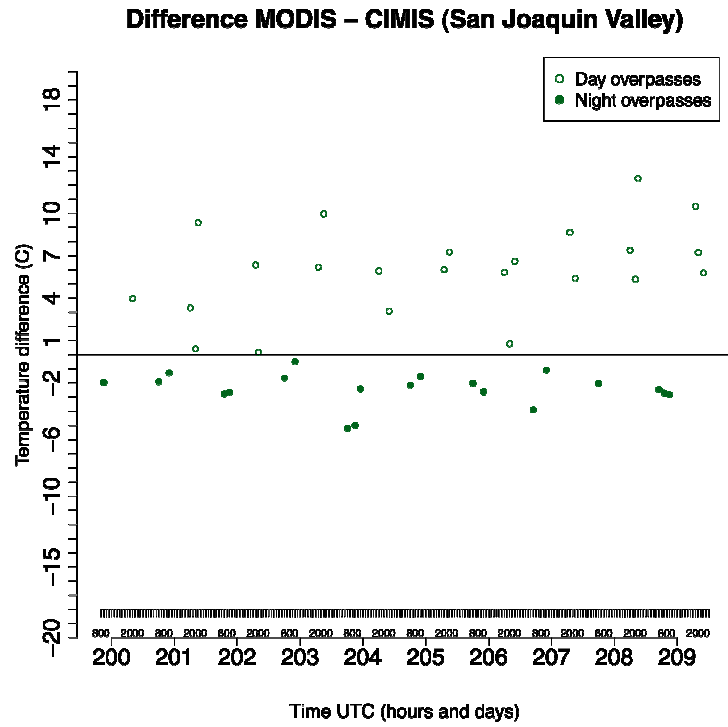
that from one cycle to another (one day to another) the overnight minimum does not go back to its previous value but also rises by a few degrees. Therefore, the next day, the radiational heating adds to a hotter initial temperature. A hotter overnight minimum temperature yields a hotter subsequent maximum. The lack of hourly data for T_{skin} does not allow for a comparison of the complete temperature-radiation cycles of air and skin temperatures but the convenient times of the MODIS overpasses within a few hours of the daily temperature extremes provides us with some information about their range. Thus, for a same initial overnight minimum temperature, T_{skin} reaches higher values than T_a . Thus, at night, when the net radiation at the surface is negative as seen on Figure 32, the difference between T_{skin} and T_a is small and even changes sign from one region to another (Figure 31 and Figure 33, filled circles) whereas near mid-day ($T_{\text{skin}} - T_a$) is larger with T_{skin} higher than T_a , as observed in previous studies (Jin et al., 1997; Zaitchik et al., 2006) and on Figure 33 (open circles). The diurnal temperature range of T_{skin} is therefore larger than T_a . This increase in ($T_{\text{skin}} - T_a$) with increasing temperatures is explained (Zaitchik et al., 2006) with the high temperature gradient that establishes near the surface during hot, clear-sky days, due to the intense heating of the surface. In Figure 32 for a same range of the net radiation measured at the surface, the resulting increase in 2m-air temperature is higher in the San Joaquin Valley than in the Central Coast Valleys. Indeed, the fog and low stratus clouds generated by the differential heating of the land and sea surfaces as well as the mixing of the air by the sea breeze, limit the build-up of the temperature in the coastal areas. The land surface temperature (skin temperature), not as affected by these processes, does not show such differences between inland and coastal regions. Figure 31 shows that the time series of skin temperature (color dots)

are very similar for the San Joaquin Valley and the Central Coast Valleys regions with comparable amplitudes, just a few degrees lower in the Central Coast.

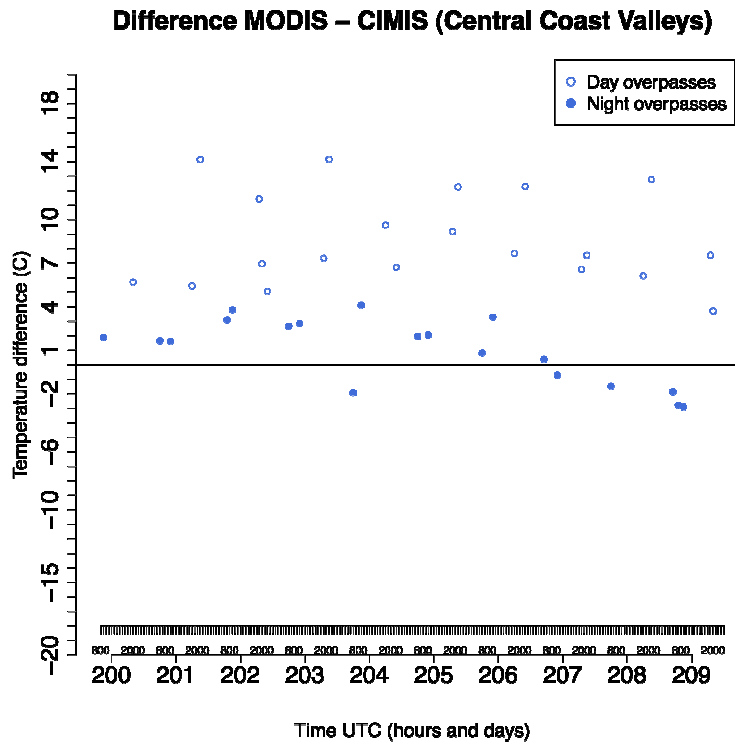
In Figure 34, T_a is plotted against T_{skin} for all the MODIS overpasses available at all stations in the San Joaquin Valley (a) and of the Central Coast Valleys (b) in order to quantify the correlation between T_a and T_{skin} for each of these regions. The observations retrieved during the night overpasses of MODIS are represented as filled squares and the day retrievals are represented with open triangles.

The significance of the relations found with the scatterplots on Figure 34 for the 4 comparisons carried out (T_{skin} versus T_a in the San Joaquin Valley at day and at night, T_{skin} versus T_a in the Central Coast Valleys at day and at night) are tested using the simple statistical test of Pearson. The four relations are found significant at the 0.01 level.

For the San Joaquin Valley, T_{skin} and T_a are highly correlated at night with a slope close to 1. T_a and T_{skin} are close since during the night the thermal gradient in the first meters of the atmospheric boundary layer is weak. For higher temperatures, during the clear-sky hot days of the heat wave, the surface receives the solar radiation and heats up more than the air because of its very low heat capacity and because of the lack of strong winds. The thermal gradient in the lower boundary layer increases and T_{skin} becomes higher than T_a . The slope of the regression changes. This confirms the conclusion from Figure 34 according to which T_a and T_{skin} respond in different ways to other variables with which they are interconnected, such as wind, soil moisture and radiation.



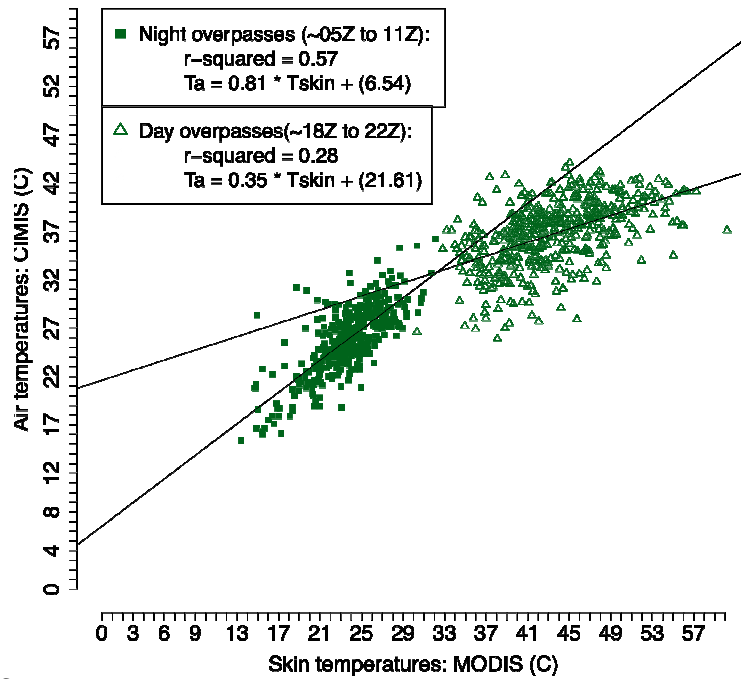
a



b

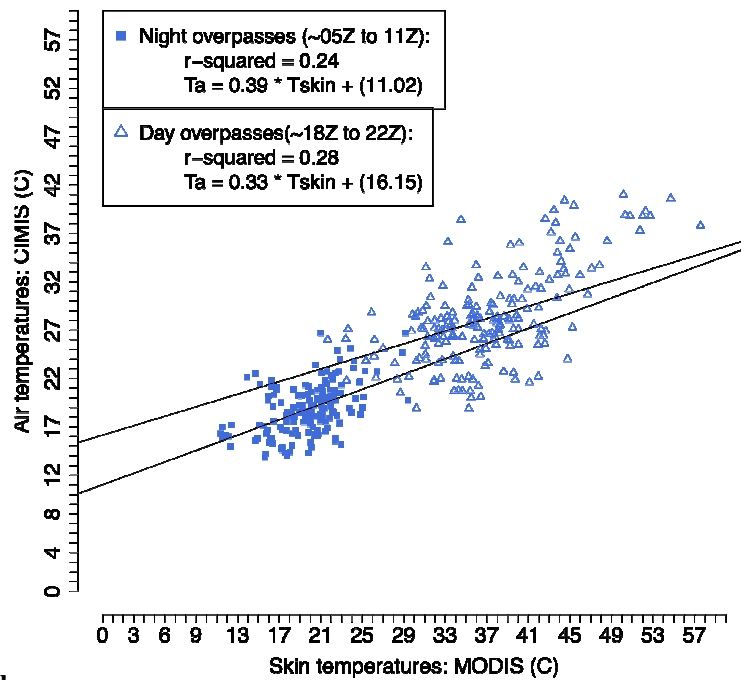
Figure 33: a, b: Difference between MODIS and CIMIS observed temperatures (MODIS-CIMIS) for daytime (open circles) and nighttime (filled circles) measurements. (a) for the San Joaquin Valley, (b) for the Central Coast Valley.

CIMIS versus MODIS data (San Joaquin Valley)



a

CIMIS versus MODIS data (Central Coast Valleys)



b

Figure 34: Scatter plots showing the relationships between T_{skin} and T_a . Correlation of the air (CIMIS) and skin (MODIS) temperatures. (c) for the regions of the San Joaquin Valley (d) for the Central Coast Valleys

The temperature in the San Joaquin Valley is affected mainly by radiation and wind. In the Central Coast Valleys, coastal phenomena such as fog, cloudiness, sea and land breezes also impact T_a with only a minor effect on T_{skin} . Therefore, the relation between the surface and air temperatures is not as easily explained by the diurnal variations in radiation and do not vary as much between day and night as is the case in the San Joaquin Valley.

5. Summary and Conclusions

The mesoscale model WRF has been used to simulate the heat wave that took place over California between the 19th and the 29th of July 2006. California includes a large variety of climate regions with different topographical settings. Two of the evapotranspiration regions defined within the CIMIS network of weather stations are the object of this study: the San Joaquin Valley, mainly protected from the marine air influence by the Coastal ranges, and the Central Coast Valleys, more readily exposed to the sea breezes.

The capture of the diurnal cycle of surface temperature at 2m is first evaluated by comparing the model's results with the measurements from the CIMIS weather stations distributed over California. Averaged over the stations of the San Joaquin Valley and the Central Coast Valleys, WRF is found have a warm bias over these two regions. In both regions, the error increases with the development of the heat wave and peaks for the day of maximum temperature. In the San Joaquin Valley, this error shows a daily cycle with a minimum during the morning and then remains maximum

during the night cooling that is started later by WRF than in the observations. This lag in the temperature decrease is associated with a delay in the decay of the sea breeze.

In the Central Coast Valleys, the error has less of a diurnal cycle than in the San Joaquin Valley and the sea breeze onset and decay times are better captured. The temperature errors increase during the development of the heat wave.

The spatial distribution of the modeling errors is then analyzed by comparing the modeled skin temperature with the land surface temperature retrieved by the MODIS sensors. It is found that the error in the modeling of the skin temperature is related to the land cover and the soil moisture. Soil moisture is evaluated by comparison with the results from a 24-month LIS simulation. Some errors due to the land cover are due to misclassifications, partly due to the lack of classes to represent accurately the variety of vegetation species. The Central Coast of California is a good example of this type of misclassification. The USGS land cover dataset does not include the small-scale changes in vegetation and the area is uniformly classified as savanna when there are actually croplands, conifers, woodlands and chaparral. Depending on the type of misclassification, the bias can be cold or warm. For example, conifers classified as savanna yield a cold bias but croplands and woodlands yield a cold bias during the day and warm bias at night.

The soil moisture is also related with the temperature biases. The soil water content due to the irrigation along the axis of the Central Valley is not captured neither by LIS nor by WRF, and yields a warm bias of the skin temperature. The coniferous mountains and ranges north and east of the Central Valley are simulated with a wet bias and the associated temperature has a warm bias during the day and cold bias during the night.

Skin temperature and surface air temperature are two quantities that do not respond to changes of the environment in the same way. The skin temperature is more sensitive to increases in radiation than surface air temperature. The relationship of skin and air temperature also changes with the location. In the Central Coast Valleys air temperature is more sensitive to small changes in wind speed than in the San Joaquin Valley. In the San Joaquin Valley, the surface air temperature and the skin temperature are very close at night. During the day, the skin temperature responds fast to changes in radiation and therefore increases more than air temperature changing the relation between air and skin temperatures. In the Central coast Valleys, the effect of the change in radiation on skin temperature is mitigated by the wind variability and the relationship between air and skin temperature does not clearly change between day and night.

The strengths and weaknesses of WRF used to model a heat wave situation have evaluated. The use of combined satellite and stations data provides observations data at high spatial and temporal resolutions to allow a thorough evaluation of the model accuracy. WRF has significant biases representing the surface temperature and wind flow over the San Joaquin Valley during a severe heat wave. Some of the problems might be resolved by a better representation of the soil moisture, wetter in the irrigated areas and drier in the non irrigated areas. Improvement might also occur for some areas where WRF uses the wrong vegetation type.

6. References

- Adegoke, J.O., Pielke, R.A., Eastman, J., Mahmood, R. and Hubbard, K.G., 2003. Impact of Irrigation on Midsummer Surface Fluxes and Temperature under Dry Synoptic Conditions: A Regional Atmospheric Model Study of the U.S. High Plains. *Monthly Weather Review*, 131(3): 556-564.
- Beniston, M., 2004. The 2003 heat wave in Europe: A shape of things to come? An analysis based on Swiss climatological data and model simulations. *Geophys. Res. Lett.*, 31.
- Blier, W., 2007. The record breaking central California heat wave of July 2006, 22nd Conference on Weather Analysis and Forecasting/18th Conference on Numerical Weather Prediction, Park City, UT.
- Caldwell, P., Chin, H.-N., Bader, D. and Bala, G., 2009. Evaluation of a WRF dynamical downscaling simulation over California. *Climatic Change*, 95(3): 499-521.
- Case, J.L., Crosson, W.L., Kumar, S.V., Lapenta, W.M. and Peters-Lidard, C.D., 2008. Impacts of High-Resolution Land Surface Initialization on Regional Sensible Weather Forecasts from the WRF Model. *Journal of Hydrometeorology*, 9(6): 1249-1266.
- Case, J.L., LaCasse, K.M., Santanello, J.A., Lapenta, W.M. and Peters-Lidard, C.D., 2007. Improved modeling of land-atmosphere interactions using a coupled version of WRF with the Land Information System. In: A.M. Society (Editor), 21st Conference on Hydrology, San Antonio, TX.
- Cheng, W.Y.Y. and Steenburgh, W.J., 2005. Evaluation of Surface Sensible Weather Forecasts by the WRF and the Eta Models over the Western United States. *Weather and Forecasting*, 20(5): 812-821.
- Chiao, S., 2006. Performance of planetary boundary layer schemes in the WRF model, 25th Army Science Conference, Orlando, FL, pp. 8.
- Chuvieco, E. and Justice, C., 2008. NASA Earth Observation Satellite Missions for Global Change Research, *Earth Observation of Global Change*, pp. 23-47.
- D'Andrea, F., 2007. Hot European Summers: the propagation of Mediterranean drought, 2nd ESF MedCLIVAR workshop - Connections between Mediterranean and Global Climate Variability, La Londe les Maures, Toulon, FRANCE.
- Easter, J., 2004. California Vegetation/Wildlife Habitat Regions.
- Ek, M.B. et al., 2003. Implementation of Noah land surface model advances in the National Centers for Environmental Prediction operational mesoscale Eta model. *J. Geophys. Res.*, 108.
- Fink, A.H. et al., 2004. The 2003 European summer heatwaves and drought -synoptic diagnosis and impacts. *Weather*, 59(8): 209-216.
- Fischer, E.M., Seneviratne, S.I., Vidale, P., Luthi, D. and Schar, C., 2007b. Soil Moisture-Atmosphere Interactions during the 2003 European Summer Heat Wave. *Journal of Climate*, 20(20): 5081-5099.
- Fovell, R., 2008. Validation of WRF Surface Meteorology Simulations, presentation, 4 November 2008, CCOS Technical Committee Meeting, California Air Resources Board, Sacramento.

- Gershunov, A. and Cayan, D., 2008. Recent Increase in California Heat Waves: July 2006 and the last six decades. California Energy Commission, PIER Energy-Related Environmental Research, CEC-500-2008-088.
- Gershunov, A., Kanamaru, H., Knowles, N., Kanamitsu, M. and Cayan, D., 2006. Weather and climate extremes over California topography: precipitation and temperature in observations and regional modeling, MTNCLIM 2006 Conference, Mt Hood, Oregon, USA.
- Grotjahn, R., 2009. Using extreme heat waves to downscale large scale upper air data to California Central Valley summertime maximum surface temperatures, submitted to Climate Dynamics.
- Grotjahn, R. and Faure, G., 2008. Composite Predictor Maps of Extraordinary Weather Events in the Sacramento, California, Region. *Weather and Forecasting*, 23(3): 313-335.
- Hart, Q.J. et al., 2008. Daily reference evapotranspiration for California using satellite imagery and weather station measurement interpolation. *Civil Engineering and Environmental Systems*, 26(1): 19-33.
- Hohenegger, C., Brockhaus, P., Bretherton, C.S., Sch and r, C., 2009. The Soil Moisture-Precipitation Feedback in Simulations with Explicit and Parameterized Convection. *Journal of Climate*, 22(19): 5003-5020.
- Hong, S.-Y. and Lim, J.-O.J., 2006. The WRF single-moment microphysics scheme (WSM6). *Journal of the Korean Meteorological Society*, 42: 129-151.
- Hong, S., Lakshmi, V. and Small, E.E., 2007. Relationship between Vegetation Biophysical Properties and Surface Temperature Using Multisensor Satellite Data. *Journal of Climate*, 20(22): 5593-5606.
- IPCC, I.P.o.C.C., 2007. Climate Change 2007: Synthesis Report; Summary for Policymakers.
- Janjic, Z.I., 2002. Nonsingular Implementation of the Mellor-Yamada Level 2.5 Scheme in the NCEP Meso model.
- Jin, M., Dickinson, R.E. and Vogelmann, A.M., 1997. A Comparison of CCM2-BATS Skin Temperature and Surface-Air Temperature with Satellite and Surface Observations. *Journal of Climate*, 10(7): 1505-1524.
- Kozlowski, D.R. and Edwards, L.M., 2007. An Analysis and Summary of the July 2006 Record-Breaking Heat Wave Across the State of California, NOAA Western Regional Tech Attach, No. 07-05 (February 27, 2007), Salt Lake City, Utah.
- Kumar, S.V. et al., 2006. Land information system: An interoperable framework for high resolution land surface modeling. *Environmental Modelling & Software*, 21(10): 1402-1415.
- Loveland, T.R. et al., 1995. Seasonal Land-Cover Regions of the United States. *Annals of the Association of American Geographers*, 85(2): 339-355.
- Mahrt, L. and Ek, M., 1984. The Influence of Atmospheric Stability on Potential Evaporation. *Journal of Applied Meteorology*, 23(2): 222-234.
- Meehl, G.A. and Tebaldi, C., 2004. More Intense, More Frequent, and Longer Lasting Heat Waves in the 21st Century. *Science*, 305(5686): 994-997.
- Michelson, S.A. and Bao, J.-W., 2006. Comparison of WRF and MM5 simulations for air-quality applications, 14th Joint Conf. on Applications of Air Pollution Meteorology and the Air and Waste Management Association,. American Meteorological Society, Atlanta, GA.
- Mitchell, K.E. et al., 2004. The multi-institution North American Land Data Assimilation System (NLDAS): Utilizing multiple GCIP products and

- partners in a continental distributed hydrological modeling system. *J. Geophys. Res.*, 109, D07S90, doi:10.1029/2003JD003823..
- Mostovoy, G. and Anantharaj, V., 2007. Sensitivity of local surface weather forecasts to initial soil moisture fields: case study over the Mississippi Delta region. In: A.M. Society (Editor), 21st Conference on Hydrology, San Antonio, TX.
- Norman, J.M. and Becker, F., 1995. Terminology in thermal infrared remote sensing of natural surfaces. *Agricultural and Forest Meteorology*, 77(3-4): 153-166.
- Norman, J.M., Divakarla, M. and Goel, N.S., 1995. Algorithms for extracting information from remote thermal-IR observations of the earth's surface. *Remote Sensing of Environment*, 51(1): 157-168.
- Prigent, C., Aires, F. and Rossow, W.B., 2003. Land surface skin temperatures from a combined analysis of microwave and infrared satellite observations for an all-weather evaluation of the differences between air and skin temperatures. *Journal of Geophysical Research (Atmospheres)*, 108, 4310-4321, 2003..
- Sauter, B. and Henmi, T., 2004. Average Forecast Errors Using MM5 and WRF Over Complex Terrain: Utah, July/August 2003 and January/February 2004. ARL-MR-597, U.S. Army Research Laboratory, White Sands Missile Range, NM.
- Sertel, E., Robock, A. and Ormeci, C., 2009. Impacts of land cover data quality on regional climate simulations. *International Journal of Climatology*, (in press)
- Skamarock, W.C. et al., 2005. A description of the Advanced Research WRF Version 2, NCAR Tech Notes-468+STR.
- Thenkabail, P.S. et al., 2009. Global irrigated area map (GIAM), derived from remote sensing, for the end of the last millennium. *International Journal of Remote Sensing*, 30(14): 54.
- Wan, Z. and Dozier, J., 1996. A generalized split-window algorithm for retrieving land-surface temperature from space. *Geoscience and Remote Sensing, IEEE Transactions on*, 34(4): 892-905.
- Zaitchik, B.F., Macalady, A.K., Bonneau, L.R. and Smith, R.B., 2006. Europe's 2003 heat wave: a satellite view of impacts and land-atmosphere feedbacks. *International Journal of Climatology*, 26(6): 743-769.
- Zampieri, M. et al., 2009. Hot European Summers and the role of soil moisture in the propagation of Mediterranean drought. *Journal of Climate*, 22(18): 4747-4758.

Appendix

6.1. Appendix1: Atmospheric humidity during the 2006 heat wave in California

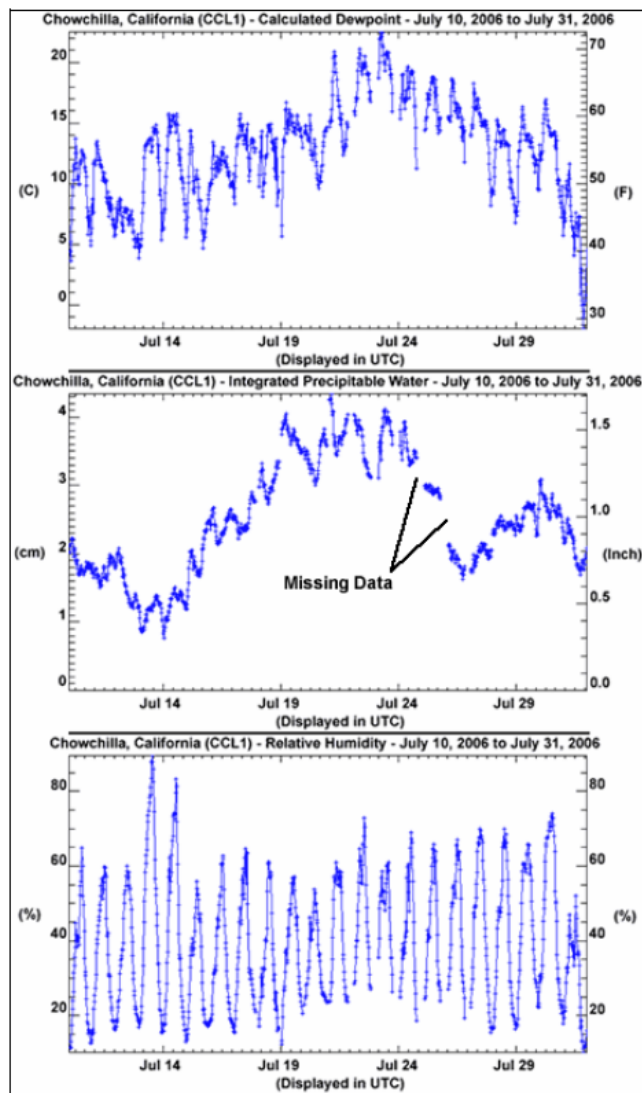


Figure 16: Depicts three unique moisture parameters, surface dew point temperature, integrated precipitable water, and relative humidity at Chowchilla, California (north-central San Joaquin Valley) from July 10 through July 31. Notice the increase of surface dew point temperature and integrated precipitable water values during the peak of the heat wave event. Also, notice the lack of change in relative humidity, except for typical diurnal fluctuations.

Figure 35: from (Kozlowski and Edwards, 2007) . Air moisture indicators at the Chowchilla station

6.2. Appendix 2: Event identification

A preliminary analysis of the temperatures during the summer 2006 is carried out to identify the period of study.

Long term daily means

A climatology of the daily maximum temperatures is first calculated for each of the 118 stations of the network with at least 10 years of data records available. This climatology consists of long term daily means (LTDM) calculated by averaging for each station the maximum (resp. minimum) temperatures recorded on 7 consecutive days (3 before and 3 after) of the JJA period of each year. For each station, these daily averaged temperature profiles are then fitted to cubic polynomial functions to remove the interannual variability due to the small number of years used to calculate the long term means.

Four examples of these LTDM and their fit are presented in Figure 35 to Figure 38.

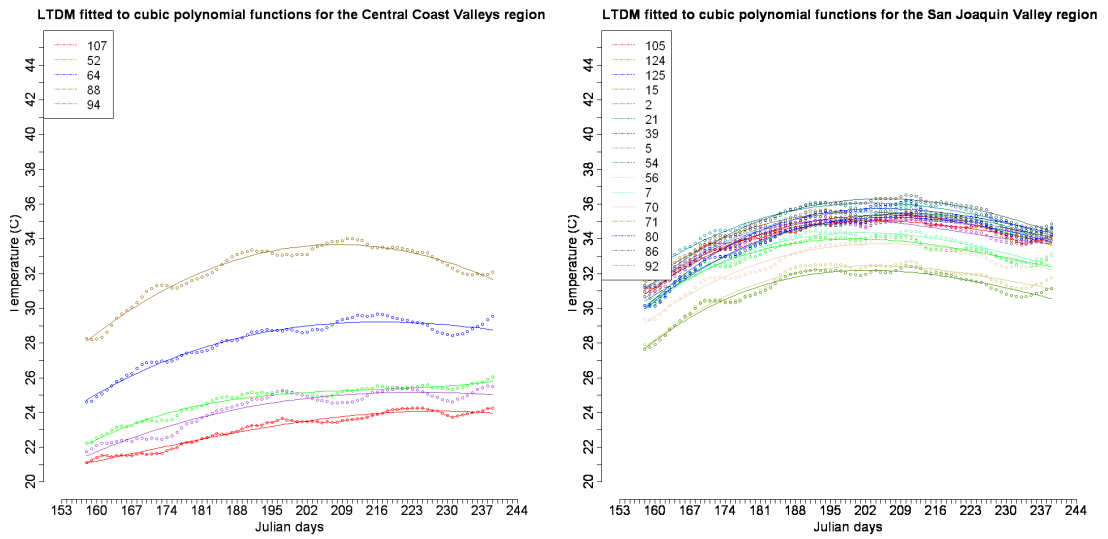


Figure 36: Long Term Daily Means for the stations of the Central Coast Valleys

Figure 37: Long Term Daily Means for the stations of the San Joaquin Valley region

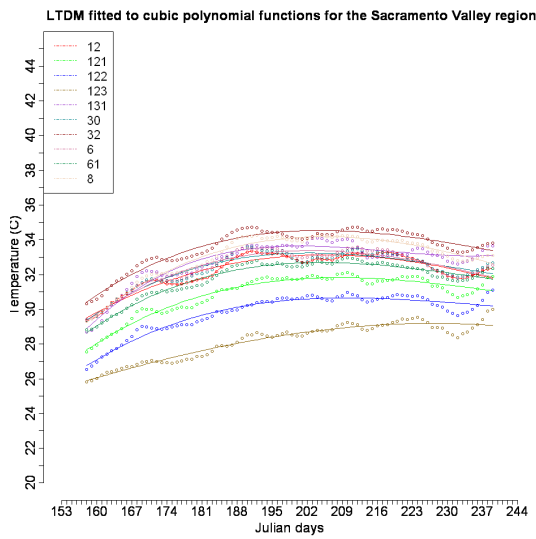


Figure 38: Long Term Daily Means for the stations of the Sacramento Valley region

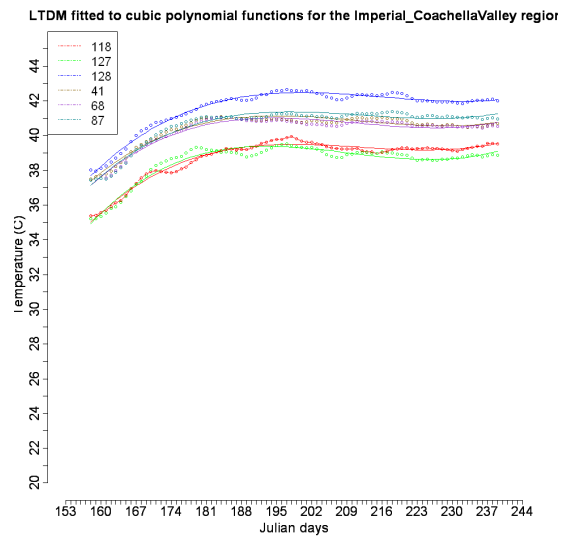


Figure 39: Long Term Daily Means for the Imperial Coachella Valley region

Anomaly profiles

From these climatological datasets, for each day of the 2006 JJA period, the departure from the LTDM is then derived yielding 2006 temperature anomaly profiles for each station which are plotted by climate regions.

Figure 40 shows the daily maxima temperature anomaly profiles obtained for the stations of the Central Valley region. Two features appear as unusually hot events between the 21st of June (day 172) and 30th of July (day 181) (period 1) and between the 19th of July (day 200) and the 29th of July (day 210) (period 2).

For this study, a heat wave event is identified when at least 3 consecutive days reach a maximum temperature anomaly of 5C with at least one day with an anomaly above 7C.

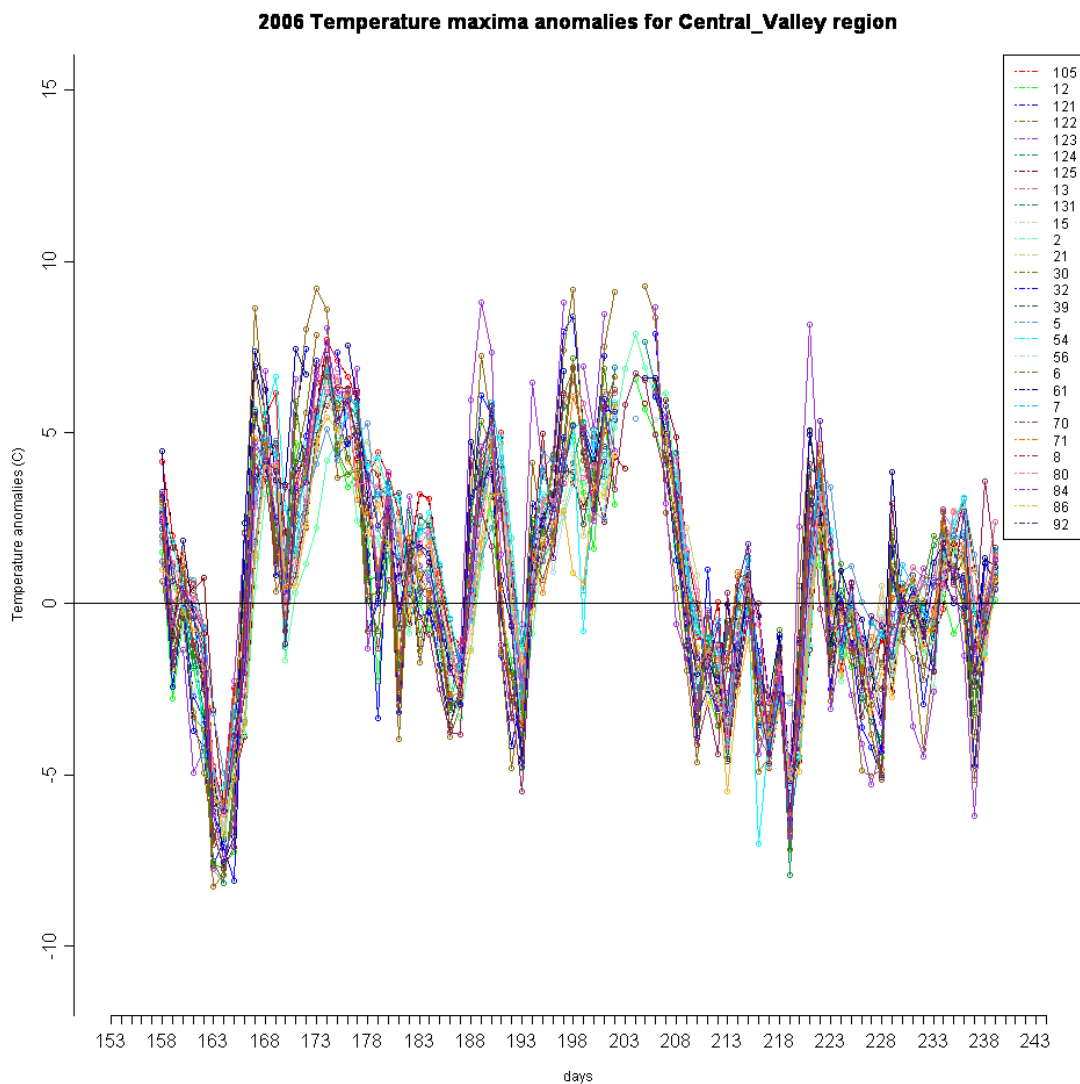


Figure 40: Anomaly profile for Daily maxima temperatures for the stations of the Central Valley region including the stations of the San Joaquin and the Sacramento Valleys (y-axis is Temperature anomaly in °C, x-axis is the 2006 Julian day or which the anomaly is calculated)

According to this definition of a heat wave, period 2 is identified as a heat wave (HW2) for more stations than period 1 (HW1) (period 1 is identified as a heat wave for 80 stations out of 118, period 2 is identified as a heat wave for 106 stations out of 118).

Also, out of all of the 118 stations, 25 reached their maximum anomaly of the 2006 summer during period 1, 90 reached their maximum anomaly of the 2006 summer during period 2 and only 3 have maximum out of these 2 periods. Out of the stations where the temperature anomaly met the criterion for HW1, all but one had temperature anomalies also identifying a heat wave for HW2. However, out of the stations where HW2 was identified as a heat wave, HW1 did not seem to meet the criterion for heat wave identification in the Coastal regions, especially in the Central and North Coast regions with only 7 out of 25 stations where the heat wave has been identified.

Also, the absolute temperatures recorded for the second event were higher due to its time of occurrence at the end of July.

Based on these observations, it appears that the second heat wave had a stronger impact over the state and the 10 days during which most of the maxima have been recorded will therefore be chosen for the time period of the study: 19th to 29th of July 2006.

6.3. Appendix 3: CIMIS network of weather stations

The CIMIS network of weather stations is organized in regions based on evapotranspiration characteristics, climate and topography (Figure 41).

116 stations are used in this study.



Figure 41: CIMIS stations used in this study and definitions of the CIMIS regions

6.4. Appendix 4: Offline spin-up simulation with the LIS

The goal of the spin-up is for the Noah LSM to reach “equilibrium”, meaning that the state of the soil at the end of the spin-up has no memory of the initial first-guess fields.

Following the method used in (Case et al., 2007), test runs are run to determine the length of the spin-up necessary for the modeled soil to reach an equilibrium state. LIS is run uncoupled for durations between 3 and 30 months with a 3-months interval between 2 test runs with all of the runs ending at time 19JUL2006_00:00:00 (initial time for WRF runs).

Noah has 4 soil layers, the 4th one (100cm-200cm) is the deepest and therefore is less dependent on the atmospheric forcing and more important to determine whether the model has reached a thermal equilibrium.

The initial condition imposed on all 4 levels of Noah consists of a uniform soil temperature of 290K and volumetric soil moisture of 30%. The LSM is then forced with North American Land Data Assimilation System atmospheric data for the upper boundary and the lower boundary is forced with a constant temperature of 290K.

The final soil moisture fields in the 4th layer of the model of each run are compared 2 by 2 to evaluate the evolution of the model with the length of the runs (Figure 42).

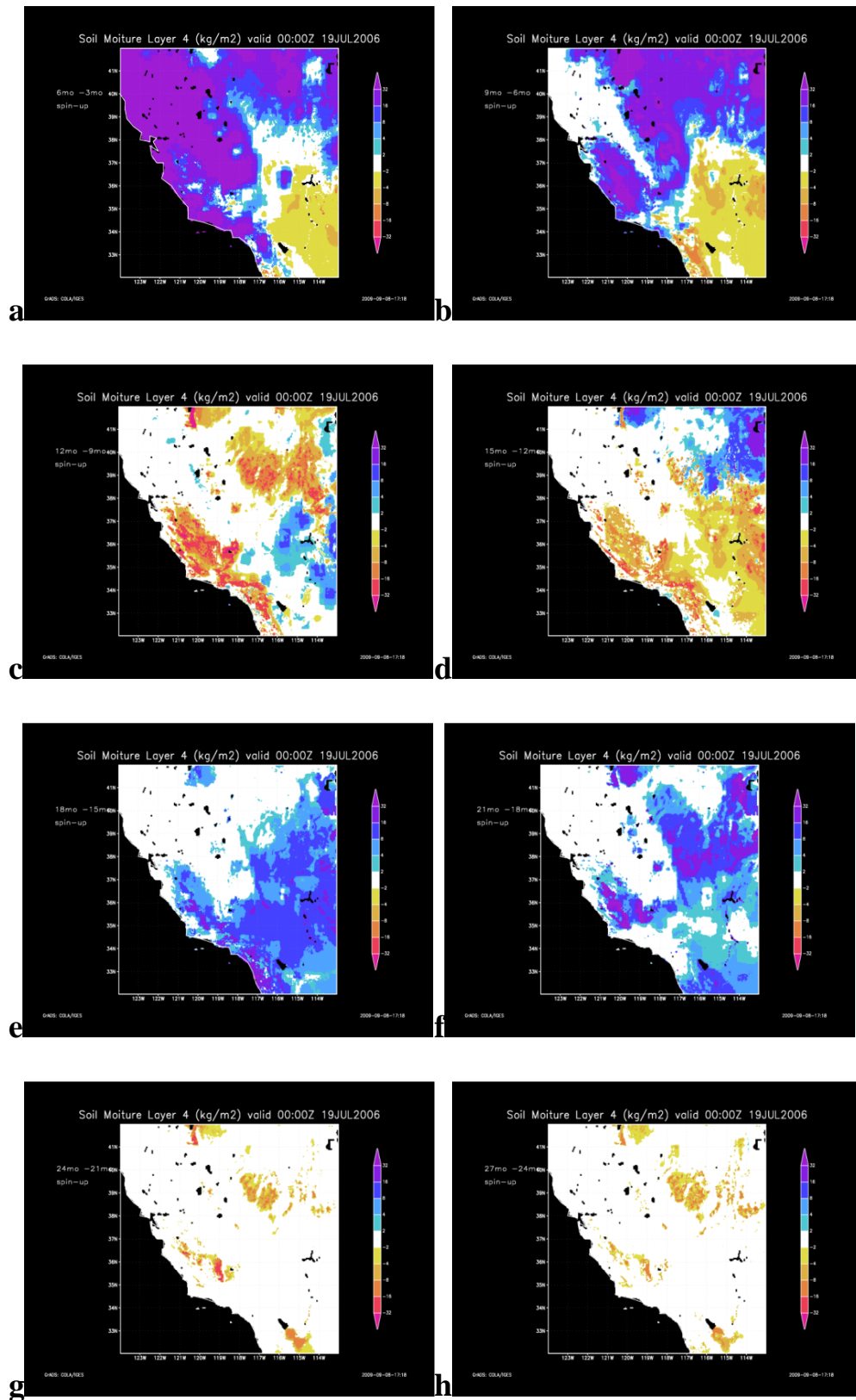


Figure 42: Difference fields between two successive offline LIS spin-up simulations of layer 4 volumetric soil moisture in the NOAH LSM, valid at 00UTC 19 Jul 2006 for:: a) 6months - 3months simulation, b) 9months - 6months simulation, c) 12months - 9months simulation, d) 15months - 12months simulation, e) 18months - 15months simulation, f) 21months - 18months simulation, g) 24months - 21months simulation, h) 27months - 24months simulation.